Photoconductive heater-detectors for photonic integrated circuits

by

Connor Mosquera

B. Eng, Carleton University, 2018

A THESIS SUBMITTED IN PARTIAL FULFILLMENT
OF THE REQUIREMENTS FOR THE DEGREE OF

Masters of Applied Science

in

THE FACULTY OF GRADUATE AND POSTDOCTORAL STUDIES
(Electrical and Computer Engineering)

The University of British Columbia
(Vancouver)

December 2020

The following individuals certify that they have read, and recommend to the Faculty of Graduate and Postdoctoral Studies for acceptance, the thesis entitled:

Photoconductive heater-detectors for photonic integrated circuits

submitted by **Connor Mosquera** in partial fulfillment of the requirements for the degree of **Masters of Applied Science** in **Electrical and Computer Engineering**.

Examining Committee:

Lukas Chrostowski, Electrical and Computer Engineering
Supervisor

Sudip Shekhar, Electrical and Computer Engineering
Committee Member

Jeff Young, Physics and Astronomy
Committee Member

Abstract

Electro-optic feedback control is an active research area within integrated photonics, where detection and tuning elements are used to dynamically control devices and circuits. However, the need for discrete control elements increases the number of electrical connections to a photonic chip, and can require large area on-chip to integrate. Therefore, a single element that can perform both detection and tuning would provide great benefit over their disjoint counterparts as photonic circuit density increases. Photoconductive heater-detectors (PCHD) have proven viable as a hybrid control and detection element, but the lack of models available make it unlikely for circuit designers to adopt them in their designs.

We propose an empirical compact model for PCHDs based on measured results. Core electro-optic relationships are pulled from literature and empirically modeled. A compact model for the general structure of a PCHD is implemented in Lumerical INTERCONNECT using standard library elements populated with parameters specific to the n-doped PCHDs that were measured. The compact model is used in a variety of simulations and compared against measured results.

We also demonstrate the design of a widely tunable ring-based silicon photonic notch filter. We present measured results demonstrating the device capability of tuning the filtering frequency, the free spectral range (two states), the optical bandwidth from 5 to 34 GHz, and the extinction ratio in excess of 30 dB, all independently of each other. We also provide circuit simulations using the PCHD model to demonstrate feedback loops used to automatically reconfigure the circuit based on specific spectral property optimizations.

Lastly, we propose an advanced silicon photonic biosensor architecture for the detection of COVID-19 and other pathogens, enabled by PCHDs. By integrating

the detector and tuner as a single element within the resonant cavity and operating in the O-band rather than the C-band, cheap single wavelength lasers can be used as an optical source rather than the standard sweepable lasers required to operate photonic biosensors. Simulated results of the sensor highlight the trade-off between environmental sensitivity and measured signal strength as the size of the sensing region increases.

Lay Summary

Silicon photonics is a quickly developing technology platform that can be used to create large electro-optic circuits for a variety of applications. An important component in these circuits are photoconductive heater-detectors, which can be used to simultaneously detect and alter optical signals. This functionality allows for automated control of circuit elements through feedback control loops while taking up less space in a circuit than alternative devices. We have developed a model for the electro-optic properties of these devices based on measured results from fabricated test structures, allowing designers to estimate the performance of these devices in their circuits before fabrication. We also demonstrate target applications for such devices through simulation and measurement, including a compact and widely reconfigurable filter, and an advanced silicon photonic biosensor with application to the detection of COVID-19.

Preface

The content of this thesis is based on two publications, listed below, in which I am the principal author. Chapter 2 is based on the following invited publication (to be submitted):

1. C. Mosquera, H. Shoman, S. Shekhar, and L. Chrostowski, "Doped silicon in-waveguide heaters for tuning and detection in photonic circuit applications," *SPIE Photonics West*, 2021.

I am the main contributor to this publication. L. Chrostowski conceived the idea. I designed the model structure, and implemented it into software. H. Shoman performed measurements of fabricated devices. I analyzed the data, extracted device parameters, and performed analysis to compare the model to measured results. I wrote the manuscript, with editing help from H. Shoman, S. Shekhar, and L. Chrostowski.

Chapter 3 is based on the previous publication, as well as the following publication [1]:

1. C. Mosquera, H. Shoman, and L. Chrostowski, "A tunable optical notch filter on SOI platform," *IEEE Photonics Conference*, 2020.

I am the main contributor to this publication. H. Shoman conceived the idea. H. Shoman designed the fabricated circuits. I performed measurements of fabricated circuits. I analyzed the data and extracted performance metrics. H. Shoman and I wrote the manuscript, with editing help from L. Chrostowski.

Chapter 4 is based on unpublished work, to be published at a later date.

Table of Contents

Abstract . . . . . **iii**

Lay Summary . . . . . **v**

Preface . . . . . **vi**

Table of Contents . . . . . **vii**

List of Tables . . . . . **x**

List of Figures . . . . . **xi**

Glossary . . . . . **xiv**

Acknowledgments . . . . . **xvi**

1 Introduction **1**

1.1 Silicon Photonics 1

1.2 Electro-Optic Control 2

1.3 Photoconductive Heater-Detectors 3

1.4 Thesis Organization 4

2 Photoconductive Heater-Detector Modeling **5**

2.1 Device 5

2.2 Optical Properties 6

2.2.1 Propagation Loss 7

2.2.2 Index and Phase . . . 7
2.3 Electrical Properties . . . 7
2.3.1 Dark Current . . . 8
2.3.2 Photocurrent . . . 8
2.3.3 Noise . . . 12
2.3.4 Detection and Tuning Bandwidth . . . 12
2.4 Compact Model . . . 12
2.5 Simulation Results . . . 15
2.5.1 Responsivity and Noise . . . 15
2.5.2 Modulation . . . 17
2.5.3 In-Resonator Configuration . . . 18
2.6 Summary . . . 21

3 Application - Notch Filter . . . 22
3.1 Ring Resonator Theory . . . 23
3.1.1 Extinction Ratio and Bandwidth . . . 24
3.2 Operating Principle and Design . . . 25
3.3 Experimental Characterization . . . 26
3.4 Detect and Tune . . . 27
3.5 Summary . . . 30

4 Application - Biosensor . . . 31
4.1 Sensor Architecture . . . 32
4.2 Performance Metrics . . . 32
4.3 Circuit Design . . . 35
4.4 Simulation Results . . . 38
4.5 Summary . . . 43

5 Conclusion . . . 45
5.1 Future Work . . . 46
5.1.1 Photoconductive Heater-Detector Model . . . 46
5.1.2 Notch Filter . . . 47
5.1.3 Biosensor . . . 47

Bibliography **49**

List of Tables

Table 2.1 Summary table of the model properties and INTERCONNECT elements used to implement them 13

Table 4.1 SWG propagation loss estimates based on [2] 39

Table 4.2 Circuit parameters and performance analysis for two circuit variants in INTERCONNECT, where reported taper losses are for individual components, and the total SWG waveguide length L_{SWG} is discretized into 120 µm sections and looped back and forth as shown in Fig. 4.4 40

List of Figures

Figure 2.1 a) PCHD waveguide geometry and doping profile and b) photoconduction process, where the generated electron and hole mobilities dictate their speeds, and charge neutrality is maintained by injection of additional electrons from the negative terminal 6

Figure 2.2 Measured dark current and power vs. voltage for a 100 µm long PCHD 9

Figure 2.3 Measured PCHD responsivity as a function of bias voltage V and optical power P_{opt} 10

Figure 2.4 Curve fits for R with respect to a) optical power P_{opt} for $V = 1\,\mathrm{V}$, and b) voltage V for $P_{opt} = -12.8\,\mathrm{dBm}$ 11

Figure 2.5 a) Block diagram of PCHD, b) top-level schematic of PCHD INTERCONNECT model, and c) sub-level schematic for determining I_{photo} 14

Figure 2.6 Comparison of measured and simulated photocurrent as a function of bias voltage and optical power 16

Figure 2.7 Comparison of measured and simulated photocurrent as a function of optical power for a 100 µm long detector biased at 1 V 16

Figure 2.8 Comparison of measured and simulated bandwidths for a) detection and b) tuning of the PCHD. Simulated signals were extracted via time-domain simulations of the device in INTERCONNECT, extracted with an oscilloscope monitor 17

Figure 2.9 a) Test circuit with PCHD placed in a microring resonator, b) simulated sweeps of the ring resonator with and without the input laser light, with the photocurrent calculated from the subtraction of the two signals 18
Figure 2.10 Comparison between in-resonator PCHD and equivalent germanium PD power tap for resonance photodetection, with a) device illustrations and b) simulation results. The germanium PD current is measured directly, resulting in a detection floor corresponding to the device dark current, while the PCHD photocurrent is calculated as the difference between the current with the laser on and off, with the detection floor corresponding to the device thermal noise 20

Figure 3.1 Add-drop ring resonator a) architecture and b) through port (solid blue) and drop port (red) transmission responses for $r_1 = r_2 = 0.9$ and $a = 0.8$, as well as through port (dashed blue) response for critical coupling with same coupling coefficients ($a = 1$) 23
Figure 3.2 The tunable notch filter. a) Schematic illustrating the filter's spectrum tailoring elements. b) Microscope image of the fabricated device. The electrical contacts (top and bottom) were wirebonded to a PCB for the electrical control. 25
Figure 3.3 Filter through-port experimental results. a) Comparison of the FSRs for the two configurations of MZI2. b) Voltage sweep of PS2 over the full FSR. 2D sweeps over MZI1 and MZI3 for a fixed MZI2 showing c) extinction ratio and d) bandwidth of the resonance at 1549.45 nm in b) (for no electrical power applied to PS2) 26
Figure 3.4 The tunable notch filter INTERCONNECT model 28
Figure 3.5 Filter tuning process used to align filter resonance wavelength to 1550 nm and maximize the extinction ratio 29

Figure 4.1 Biosensor architecture for a) a wavelength-sweepable sensor and b) a single wavelength, PCHD-sweepable sensor 33
Figure 4.2 Difference between SWG (top) and SWG-assist/fishbone (bottom) waveguides, including strip-SWG taper transitions . . . 36
Figure 4.3 Propagation loss of water as a function of wavelength [3] . . . 37
Figure 4.4 Proposed biosensor circuit layout, including a balanced MZI for tunable coupling to the resonator 38
Figure 4.5 PCHD voltage vs. photocurrent for two sensing region lengths, and two different n_{clad}, demonstrating how a longer sensing region produces weaker photocurrent peaks but strong sensitivity to environmental changes. The difference between photocurrent peaks is 25 mV and 90 mV for $L_{SWG} = 240\,\mu m$ and $L_{SWG} = 960\,\mu m$ respectively. Results are for C-band sensors. . 41
Figure 4.6 Simulation results of the 1310 nm and 1550 nm sensor circuits for a) Q and S, and b) iLoD and ER 42

Glossary

CMOS Complementary Metal-Oxide-Semiconductor

COVID-19 Coronavirus Disease 2019

EO Electro-Optic

ER Extinction Ratio

FDTD Finite-Difference Time-Domain

FSR Free Spectral Range

FWHM Full Width at Half Maximum

GWN Gaussian-Distributed White Noise

ILOD Intrinsic Limit of Detection

LIDAR Light Detection and Ranging

MZI Mach-Zehnder Interferometer

OMM Optical Modulator Measured

PCB Printed Circuit Board

PCHD Photoconductive Heater-Detector

PD Photodetector

PS Phase Shifter

TE Transverse Electric

TM Transverse Magnetic

TO Thermo-Optic

SLOD System Limit of Detection

SMU Source Measure Unit

SNR Signal-to-Noise Ratio

SOI Silicon-On-Insulator

SWG Subwavelength Grating

Acknowledgments

I would like to thank my supervisor Prof. Lukas Chrostowski for the guidance and mentorship he has given me over the course of my studies. He has been a constant source of inspiration and motivation for what can be achieved within our field, and he has enabled my professional and personal growth time and time again. I also thank Prof. Sudip Shekhar for being a great mentor and teacher, and for all the effort he made to help guide me through my work. I would also like to thank Prof. Jeff Young for graciously accepting to be part of my examining committee.

My experience at UBC was heightened and enhanced by all of my colleagues in the silicon photonics group. First and foremost I would like to thank Hossam Shoman for the countless hours of effort he put into teaching and mentoring me. His patience and guidance proved instrumental in my learning and skill development, and I am grateful to him for that. I would like to thank the rest of my colleagues at UBC who I have had the pleasure of working with and learning from, in particular, Minglei Ma, Enxiao Luan, Mustafa Hammood, Stephen Lin, Jaspreet Jhoja, Han Yun, Becky Lin, Abdelrahman Afifi, Avineet Randhawa, Leanne Dias, Hasitha Jayatilleka, and Ajay Mistry.

Above all, I would like to thank my wife Lucy for her encouragement and support. She is a role model for the value of hard work and perseverance, for which I will always be inspired.

Chapter 1

Introduction

1.1 Silicon Photonics

The field of photonic integrated circuits has matured from a promising area of research interest, to a scalable approach for next generation products in a number of industries. Silicon-on-insulator (SOI) has become a popular platform of choice due to the low cost and abundance of silicon, compatibility with complementary metal-oxide-semiconductor (CMOS) electronics, and fast fabrication times. Compared to other integrated photonic platforms, SOI's high index constrast provides a strong optical confinement. This allows nanowire waveguides to be efficiently and compactly routed for dense integration. A number of high performance active components have been demonstrated in SOI including heaters [4, 5], detectors [6], modulators [7], lasers [8, 9], and more.

The SOI platform is particularly appealing for large scale system development, as it leverages decades of development in CMOS design and fabrication to create densely integrated electronic-photonic circuits capable of solving problems that neither electronics nor photonics would be able to solve independently [10]. A variety of large-scale electro-optic systems have been demonstrated practically on SOI, with applications ranging from neuromorphic systems [10, 11], quantum computing [12, 13], programmable photonic processing [14, 15], LIDAR [16, 17], reconfigurable networks [18, 19], coherent communications [20] and more. As integrated photonic circuits continue to grow in size and scope, the need for compact

and efficient elements for automated control and programmability will continue to increase.

1.2 Electro-Optic Control

Electro-optic feedback control is an ongoing research area within integrated photonics, due to the need for tuning micron-scale photonic devices sensitive to temperature and manufacturing variations. Automated controls in integrated photonic circuits are implemented via detect-and-tune feedback loops, which require both sensing and tuning elements. On-chip sensors can be implemented in a number of different ways. A common method for implementing photodetectors in silicon has been through the monolithic integration of germanium, due to its high optical absorption for infrared wavelengths [21, 22]. However, the high temperatures typically required to grow germanium on silicon (>600 °C) [21, 22] are problematic for co-integration with CMOS devices, which can see performance degradation for high-temperature processes (>300-400 °C) [23, 24]. Alternatively, p-n or p-i-n photodiodes can be used as sensors by biasing the device to create a depletion region where light is absorbed and creates a photocurrent [25]. While detectors can be placed anywhere in a circuit to monitor optical power via power taps, this approach can increase insertion losses and thus makes them unsuitable for applications that require low-loss operation, or for densely integrated systems where footprint is an important parameter. In-resonator photodiodes using defect mediation have been demonstrated [6, 26–28] to avoid the need for power taping and to make use of the build-up of optical power in resonators. However, these devices require dedicated ion implantation steps to create enough defect states for a resolvable output signal [26, 27].

Tuning elements are key components in many large scale integrated circuit applications, such as phased array antennas, optical processors, and more [29]. Most tuning elements are implemented by leveraging either electro-optic (EO) or thermo-optic (TO) effects of silicon. EO control elements are implemented by doping the silicon waveguide, and operate via plasma dispersion. When the device is electrically biased, carriers are injected and depleted which in-turn changes the density of carriers along the waveguide's cross-section and induces a phase shift

to the propagating mode [27]. TO control elements use metal or doped silicon as a resistive heating element placed above [4, 5], parallel to [30], or within [26–28] a waveguide structure to change the refractive index of the surrounding area and create a phase shift.

1.3 Photoconductive Heater-Detectors

Having separate detection and tuning elements increases the number of electrical connections to the photonic chip in a co-integrated system (separate photonic and CMOS chips), and can occupy a large area on-chip to integrate [27]. Therefore, a single element that can perform both detection and tuning would provide great benefits (such as reduction in the overall footprint for better on-chip real estate) over their disjoint counterparts as photonic circuit density increases.

Photoconductive heater-detectors (PCHD) have proven viable as a hybrid control and detection element [31]. PCHDs are another semiconductor light manipulation and sensing approach, where a detectable current is generated due to incident photons creating an imbalance of charge carriers [32], while simultaneously heating the surrounding medium due to a large device resistance. PCHDs can be implemented through a number of methods, with demonstrations including the use of germanium [33] or p-i-p [34] structures in silicon. Alternatively, a simple n-doped architecture is also possible [31] that does not require germanium deposition or dedicated ion implantation steps, providing a more simple fabrication process. While PCHDs have been shown highly useful for tuning densely integrated circuits [35], they have not seen the same widespread adoption in electro-optic circuits compared to discrete detectors and phase-shifters. However, phase shifters and photodiodes have been extensively characterized and modeled in circuit level simulators, making it easy for circuit designers to simulate and predict the circuits performance before fabrication. Therefore, the development of a compact model for PCHDs will similarly ease the simulation of circuits that contains such elements and will enable their proliferation, especially as systems scale and become more complex.

1.4 Thesis Organization

This thesis highlights the development of a compact model for PCHDs, meant as a tool for circuit designers to assess the PCHD performance on a component and circuit level before fabrication. This model is supplemented by demonstrations of PCHDs in scaleable circuits such as filters and sensors. The remainder of this thesis is organized into three main chapters:

Chapter 2 details the development of a Lumerical INTERCONNECT compact model of a PCHD circuit element. This chapter discusses the parameter extraction from measured results, how the electro-optic device characteristics are implemented, and analysis comparing the model to measured results.

Chapter 3 shows the design of a compact, widely tunable notch filter implemented with a number of tunable couplers and phase shifters, implemented using PCHDs. Measurement results of independent bandwidth and extinction ratio tuning are presented, while simulations using the PCHD model from Chapter 2 are provided detailing how detect-and-control loops can be implemented.

Chapter 4 presents a novel electro-optic biosensor architecture implemented using cheap single-wavelength lasers rather than expensive sweepable lasers. The design considerations of the sensor are presented, including discussion on the cavity losses, waveguide sensitivity, limits of detection, and more. Full circuit level simulation results are presented, making use of the PCHD model from Chapter 2 to enable electro-optic detection.

Chapter 2

Photoconductive Heater-Detector Modeling

While PCHDs have proven useful in monitoring and configuring densely integrated circuits [35], the combination of electrical and optical properties at play have made it difficult to develop a compact model for the device. With a compact model available, designers would be able to perform device and system level simulations and better understand the expected and fabricated performance of PCHD devices, leading to increased usage within large-scale system designs.

Here we present a compact model for an n-doped silicon PCHD in Lumerical INTERCONNECT with device properties derived from experimental results. INTERCONNECT is a photonic circuit solver which provides users with a library of core components as well as third party library interoperability to model complex electro-optic circuits [36]. Lumerical is a commercial multi-physics simulation suite used ubiquitously in academia and industry for integrated photonics design, so the development of a PCHD model on this platform can be easily adopted by relevant users.

2.1 Device

Fig. 2.1a illustrates a silicon-on-insulator rib waveguide partially etched by 130 nm to form a core width of 500 nm. The silicon core is lightly n-doped (5×10^{17} cm^{-3})

and the partially etched slabs far from the waveguide core are heavily n-doped (5×10^{20} cm^{-3}). The light waveguide doping acts to both decrease the electrical resistance across the waveguide, and create bulk defect states in the waveguide core which enable photon absorption through trap-assisted Shockley-Read-Hall recombination [37] and produces a significant photocurrent, as shown in Fig. 2.1b. The heavy doping acts to create ohmic contacts where metal vias can be connected. While the model structure presented in Sec. 2.4 is generalized to any PCHD element, device performance metrics are highly dependent on the fabrication process used. All performance results presented in this section are for devices fabricated at the A*STAR AMF foundry in Singapore using 193 nm deep-UV lithography [38].

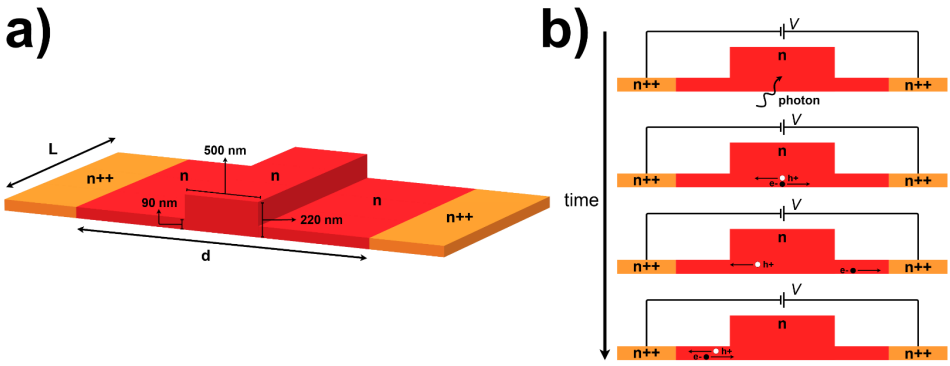

Figure 2.1: a) PCHD waveguide geometry and doping profile and b) photoconduction process, where the generated electron and hole mobilities dictate their speeds, and charge neutrality is maintained by injection of additional electrons from the negative terminal

2.2 Optical Properties

The light doping of the waveguide core is low enough to permit low-loss propagation while also creating a TO heater that changes the refractive index of the waveguide when biased, thus changing the phase of light traveling through the waveguide. The optical performance of the PCHD heater can be captured by the propagation loss and phase of the signal, which are functions of the electrical bias applied across the PCHD.

2.2.1 Propagation Loss

Propagation loss in doped SOI waveguides comes from a combination of scattering loss due to waveguide sidewall roughness and doping loss. For the devices reported here, such losses were measured to be $6.9\,\mathrm{dB/cm}$ [35], where the scattering losses were $1.9\,\mathrm{dB/cm}$ and the doping losses were $5\,\mathrm{dB/cm}$. For the purposes of this model, the total propagation losses are assumed constant with the applied electrical bias across the PCHD.

2.2.2 Index and Phase

The effective and group index for the rib waveguide geometry in Fig. 2.1 are 2.567 and 3.893 respectively, for the fundamental TE mode at a wavelength of 1550 nm, found through Lumerical MODE simulations using methods described in [39]. As the temperature of the waveguide increases, the effective index increases and creates a phase shift to the light signal passing through. Previous measurements of a PCHD in a ring resonator configuration found that as electrical power is supplied to the device, the round trip phase changed by $0.04\,\pi/\mathrm{mW}$ for a PCHD device of length $31.67\,\mu\mathrm{m}$ [40], giving a phase tuning response with respect to power and device length of $3.968\,\mathrm{rad\,mW^{-1}\,mm^{-1}}$.

2.3 Electrical Properties

The doping process used to form the PCHD creates an electrically efficient device that can be tuned over a large wavelength range while maintaining CMOS compatible voltage levels. This doping process also creates defect states in the silicon lattice of the waveguide core, which is attributed (along with surface states) to the generation of electron hole pairs and subsequent appearance of photocurrent in the presence of an optical signal. The primary properties contributing to the current output from a PCHD are: dark current due to the inherent resistivity of the device, photocurrent generated by the electron-hole pairs in the waveguide core, and current due to thermal noise. For accurate modeling, each of the aforementioned current sources are characterized and fit into the model.

2.3.1 Dark Current

Fig. 2.2 shows the dark current of a 100 µm long photoconductive heater as a function of voltage, operating at room temperature with no incident optical field. The current saturates at high voltages due to drift velocity saturation of electrons and holes for large electric fields [5, 35]. The device resistance is related to the doping and waveguide geometry in Fig. 2.1 , where the resistance is linearly proportional to the cross-sectional width between the n++ contacts d, and inversely proportional to the length of the device L. Both of these relationships can be understood through visualizing the structure as a single resistive element and picturing the doubling of d or L as the addition of another resistive element in either series (increasing d) or parallel (increasing L). The contact separation distance d should ideally be made as small as possible to increase the photoconductive gain (and thus the photocurrent), while still being cautious to avoid heavy n-doping near the waveguide core, which could otherwise significantly increase the optical losses. Thus, we set $d = 2\,\mu\text{m}$ in all fabricated devices to ensure that the highly doped regions are far enough not to interact with the optical mode propagating through the waveguide.

To model the measured dark current with the bias voltage, the function

$$I(V) = \frac{a_1 \cdot V}{a_2 \cdot V^2 + a_3} + a_4 \cdot V \tag{2.1}$$

was fit to the measured data in Fig. 2.2. This function was chosen based on the electrical power to voltage relationship in Fig. 2.2 (found through $P(V) = I(V) \cdot V$), where the power is linear for high voltages (first term in Eq. 2.1), and parabolic for low voltages (second term in Eq. 2.1). Parameter extraction was done using Matlab's "lsqcurvefit" function, which yielded coefficients for Eq. 2.1 of $a_1 = 27.58, a_2 = 333.3, a_3 = 4083, a_4 = 0.001593$.

2.3.2 Photocurrent

Detectors are characterized in part by their responsivity, R, which is the ratio of generated photocurrent I_{photo} to incident mode optical power P_{opt}:

$$R = \frac{I_{photo}}{P_{opt}} = \frac{\eta e}{hv} G_p \tag{2.2}$$

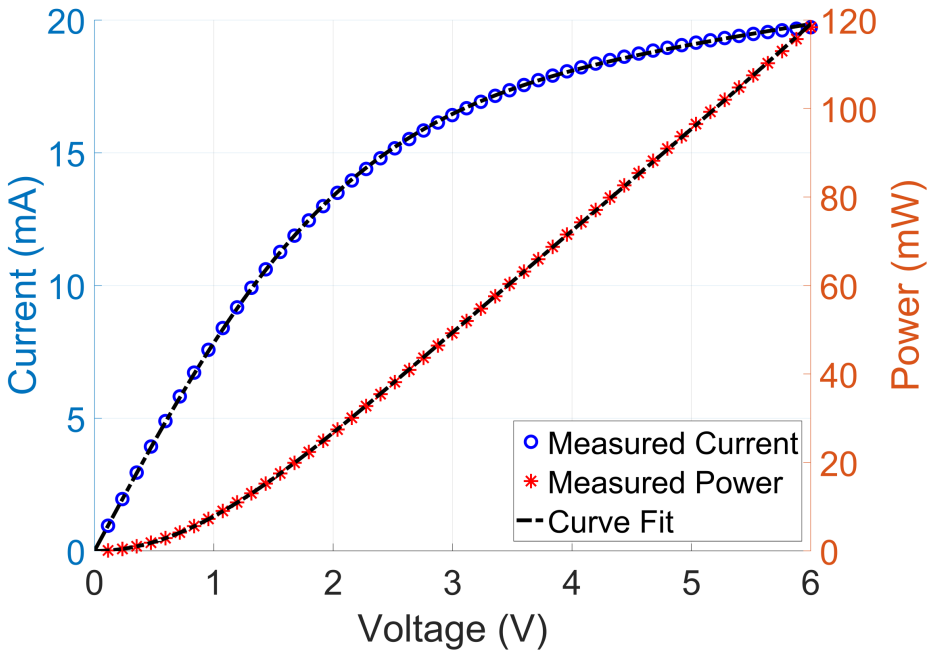

Figure 2.2: Measured dark current and power vs. voltage for a 100 µm long PCHD

where η is the quantum efficiency, e is the electron charge, hv is the photon energy, and G_p is the photoconductive gain. Photoconductive gain is the ratio of the recombination and transit times of charge carriers, which is a primary source of performance discrepancy between photodiodes and PCHDs. In photodiodes an incident photon is limited to exciting at most a single electron, meaning the range for photoconductive gains is $G_p \leq 1$. In PCHDs, minority carriers reaching the terminal have the potential to cause injection of majority carriers [32]. This means in PCHDs the effective recombination rate is much larger than that of a single carrier while the transit time remains constant, making possible much larger values of R compared to photodiodes.

Responsivity in photodiodes is typically a function of both bias voltage and optical wavelength [41], but in PCHDs the photocurrent is also dependent on the incident optical power [32]. This is attributed to the depletion rate of defect states in the PCHD being larger than the rate at which the defect states are refilled with

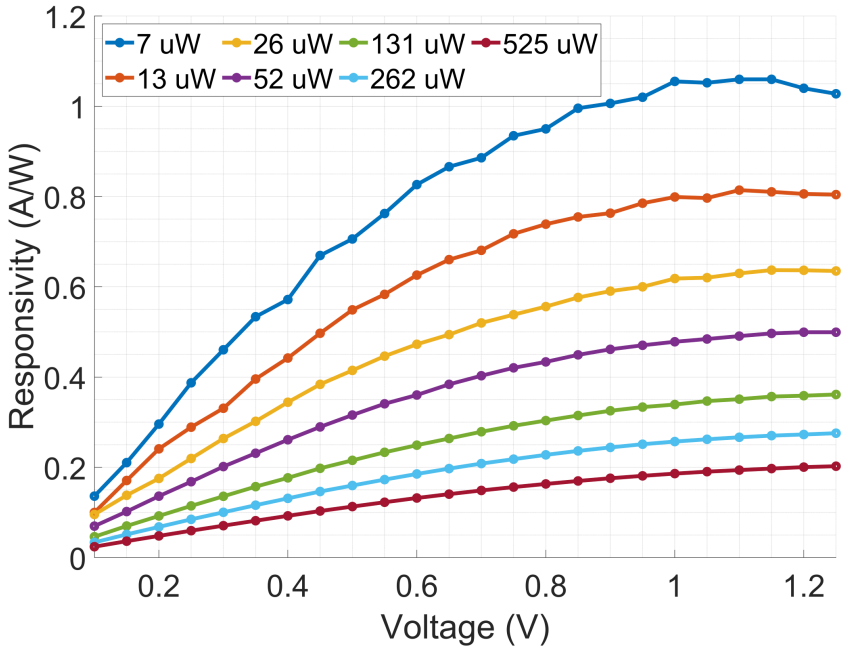

Figure 2.3: Measured PCHD responsivity as a function of bias voltage V and optical power P_{opt}

trapped carriers [40], resulting in a decrease in G_p and thus R for higher optical powers as shown in Fig. 2.3.

To generate the responsivity data for the model, the measured data was empirically curve fit to the function:

$$R(P_{opt},V) = a_1 \tanh(a_2 V) \cdot \exp(-a_3 P_{opt}) \cdot \left(1 - \frac{1}{1+\exp(-a_4 P_{opt} + a_5)}\right) \quad (2.3)$$

where P_{opt} is in units of dBm, and V is in volts. The function was selected based on observed trends in the measured data. The voltage dependence in Eq. 2.3 was selected to reflect the flattening of R with increasing voltage due to difference between electron and hole mobilities at high electric fields causing a reduction to G_p [42]. The optical dependence in Eq. 2.3 was selected to reflect the high order

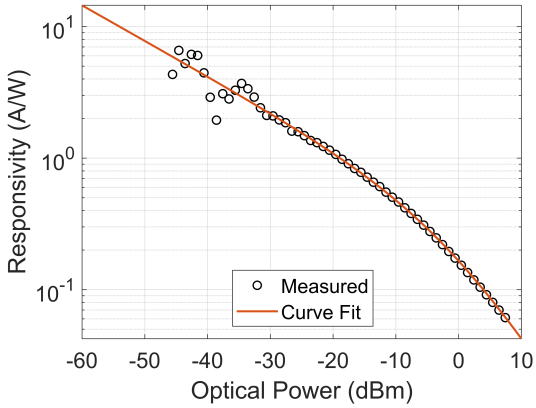

(a)

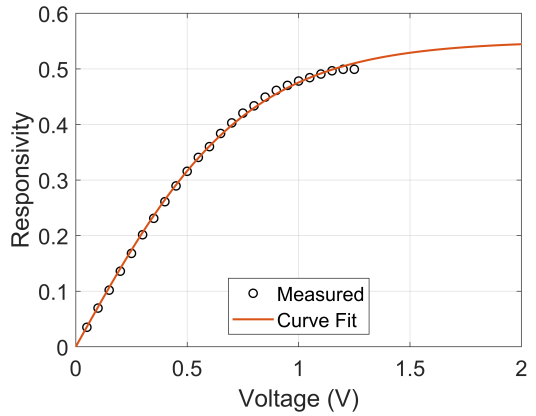

(b)

Figure 2.4: Curve fits for R with respect to a) optical power P_{opt} for $V = 1\,\text{V}$, and b) voltage V for $P_{opt} = -12.8\,\text{dBm}$

saturation of defect states in the detector for higher optical powers. A 2D curve fit to the data in Fig. 2.3 would have been the simplest method to produce a curve fit model for R, but unfortunately that measured dataset did not cover a large enough range of optical powers to capture the full nature of the higher order roll-off in I_{photo}. Instead, a two-part 1D curve fit was performed, with the results shown in Fig. 2.4. First, using a set of results of R for a large range of optical powers, Eq. 2.3 was fit while keeping V fixed at 1 V to match the bias at which the data was

measured. Similarly with voltage, the function was then fit using measured results for R as a function of V where P_{opt} was fixed at the measured optical power of -12.8 dBm. Using Matlab's "lsqcurvefit" function, coefficients for Eq. 2.3 were found as $a_1 = 0.3511, a_2 = 1.3099, a_3 = 0.0621, a_4 = 0.1123, a_5 = -0.1194$.

2.3.3 Noise

The measured current noise for this device was previously reported as $0.15\,\mu$A [35], though this was attributed as a limit of the source measurement unit used (Keithley 2602 SourceMeter) rather than the device itself. Regardless, this value was chosen to represent the noise floor of measurable current from the PCHD model, since it serves as a real limit that would be seen when using this test equipment.

2.3.4 Detection and Tuning Bandwidth

For high speed operation of the PCHD, it is important to characterize how quickly the device can detect and tune signals, effects which are captured by the detection and tuning bandwidths respectively. The detection and tuning bandwidths of this device were previously reported as 570 kHz and 175 kHz [35], corresponding to rise/fall times of 280 ns and 900 ns respectively. The detector bandwidth was measured by modulating a light source at 500 kHz and measuring the photocurrent of a PCHD placed in a ring resonator. The tuning bandwidth was measured by modulating the voltage bias of a PCHD in a Mach-Zehnder interferometer (MZI) configuration at 100 kHz and measuring the transmission signal with a photodiode. Since the detection bandwidth is much larger than the tuning bandwidth, any feedback loops implemented using this device as a detector and heater would be speed-limited by the tuning portion of the loop.

2.4 Compact Model

Tab. 2.1 summarizes the model equations and values to be used in this section. The simplest top-level diagram of the PCHD model is shown in Fig. 2.5a. The signals highlighted are an applied voltage V_{in}, an electrical current I_{total}, and optical signals P_{opt1} and P_{opt2} at both optical ports. The compact model developed in INTERCONNECT is shown in Fig. 2.5b. To incorporate the tuning bandwidth $B_t = 175$ kHz,

Table 2.1: Summary table of the model properties and INTERCONNECT elements used to implement them

Property	**Symbol**	**Value**	**INTERCONNECT component**	**Sec.**
Propagation loss	α	$6.9\,\frac{\text{dB}}{\text{cm}}$	Optical modulator measured	2.2.1
	$\frac{d\alpha}{dP}$	$0\,\frac{\text{dB}}{\text{cm}\cdot\text{W}}$		
Phase shift	$\frac{d\phi}{dP}$	$3.9968\,\frac{\text{rad}}{\text{mW}\cdot\text{mm}}$		2.2.2
Effective index	n_{eff}	2.567	MODE waveguide	
Group index	n_g	3.893		
Dark current	$I_{dark}(V)$	See Eq. 2.1	1D lookup table	2.3.1
Responsivity	$R(P_{opt},V)$	See Eq. 2.3	2D lookup table	2.3.2
Current noise	I_n	0.15 µA	GWN source	2.3.3
Tuning BW	B_t	175 kHz	Low-pass filter	2.3.4
Detector BW	B_d	570 kHz	Low-pass filter	2.5.2

V_{in} is input to a low-pass filter before being passed to the rest of the circuit. The dark current of the device I_{dark} was implemented using a lookup table populated with a high resolution table of voltages and corresponding currents from Eq. 2.1. This current is inversely scaled with L using a gain element, while d is not factored in as it is assumed as the safe value of 2 µm in fabricated devices. The optical performance of the PCHD was modeled in INTERCONNECT through a combination of the static and dynamic properties. The static optical properties of the device are determined by waveguide structure simulations performed in Lumerical MODE, and imported into the waveguide element in INTERCONNECT. This is connected in series with the "Optical Modulator Measured" (OMM) library element, which characterizes changes in the optical field due to a user defined bias such as voltage

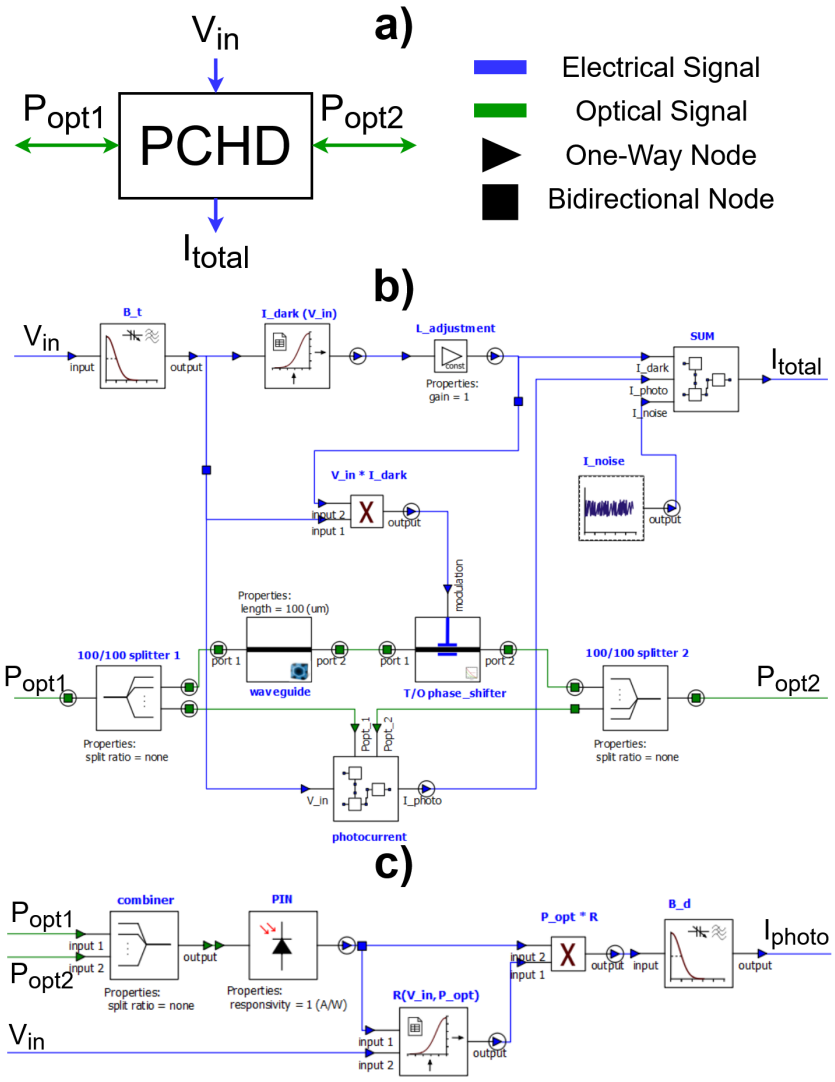

Figure 2.5: a) Block diagram of PCHD, b) top-level schematic of PCHD INTERCONNECT model, and c) sub-level schematic for determining I_{photo}

or power. In order to scale the tuning correctly with length, the bias for the OMM component was configured as a function of power, thus the given bias input is the product of V_{in} and I_{dark}.

The photocurrent block shown in Fig. 2.5c contains the sub-model used to

determine the photocurrent I_{photo}. P_{opt1} and P_{opt2} are combined (to maintain model bidirectionality) and converted to an electrical signal using a photodetector with a responsivity of 1 A/W. The optical power is then used along with V_{in} to find the corresponding responsivity R in a 2D lookup table. Data in the 2D table is made by creating a high resolution table of values from Eq. 2.3, including some extrapolation outside the range of measured data which the model is based on. Extrapolation bounds were set from -60 dBm to 10 dBm for P_{opt}, and from 0 V to 2 V for V, as shown by the figure bounds in Fig. 2.4. I_{photo} is calculated as the product of R and $P_{opt1} + P_{opt2}$. To incorporate the detection bandwidth $B_d = 570$ kHz, the signal is input to a low-pass filter before being output from the sub-model. The total current I_{total} output from the PCHD element is the sum of I_{dark}, I_{photo}, and I_{noise}, where I_{noise} is implemented using a Gaussian-distributed white noise (GWN) source with a fixed current noise of 0.15 µA.

2.5 Simulation Results

A variety of simulations were used to compare the compact model performance to measured devices. All simulation results shown here used a device length $L = 100$ µm.

2.5.1 Responsivity and Noise

Fig. 2.6 compares the measured and simulated photocurrent responses as a function of applied voltage for various optical powers. This measured data shows slightly lower photocurrents when compared to the results the model produces, which can possibly be attributed to device variations between measured results. Practically, the range of values is consistent and the overall relationship between P_{opt}, V, and R is maintained.

Fig. 2.7 provides a comparison between the measured and simulated results for the PCHD noise floor. Measured results were found by taking 50 measurements for each optical power, where the photocurrent was taken as the average and the error was taken as the standard deviation. The smallest measurable photocurrent was limited due to the measurement error of the source-measure unit used to gather the results. The deviation of the simulated results in Fig. 2.7 from the measured data

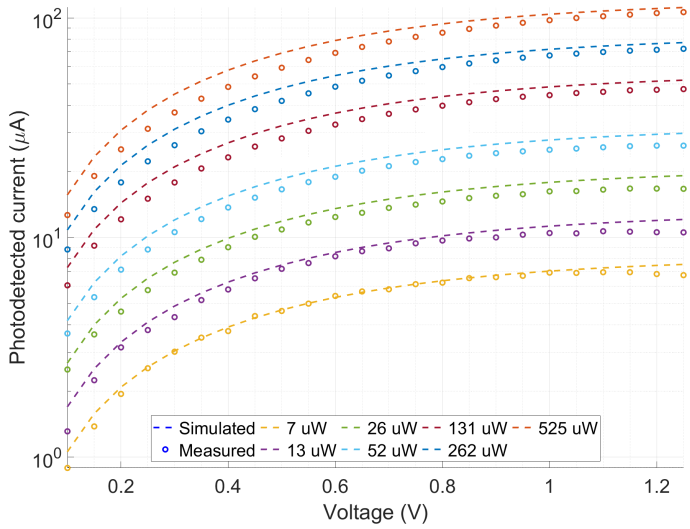

Figure 2.6: Comparison of measured and simulated photocurrent as a function of bias voltage and optical power

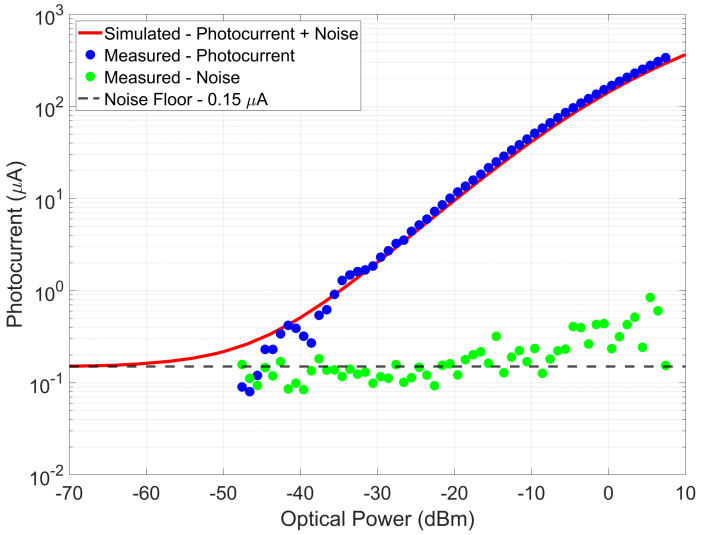

Figure 2.7: Comparison of measured and simulated photocurrent as a function of optical power for a 100 µm long detector biased at 1 V

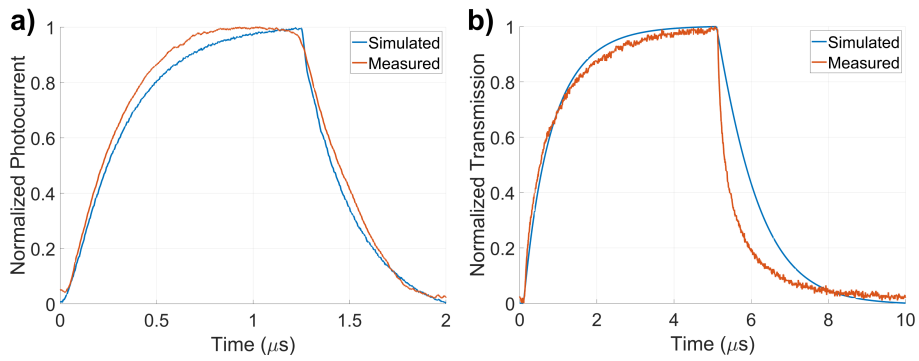

Figure 2.8: Comparison of measured and simulated bandwidths for a) detection and b) tuning of the PCHD. Simulated signals were extracted via time-domain simulations of the device in INTERCONNECT, extracted with an oscilloscope monitor

at low optical power is due to the simulated results including both the photocurrent and the noise. This measured data is the same as used for the curve fitting of R, so this plot acts as an alternative representation of the curve fit in Fig. 2.4a, where here the roll-off of photocurrent at high optical powers is visible.

2.5.2 Modulation

To observe the effect of the simulated detection bandwidth, an optical source was modulated at a frequency of 500 kHz, which was then input on a biased PCHD in a ring configuration. The resulting photocurrent was measured from the PCHD as a function of time using an oscilloscope element in INTERCONNECT, shown in Fig. 2.8a, where good agreement between the measured and simulated responses is visible. To observe the effect of the simulated tuning bandwidth, a pair of PCHD elements in an MZI configuration were biased while one was electrically modulated (in the linear region of the MZI) at a frequency of 100 kHz. The optical transmission is shown in Fig. 2.8b with the measured results, which show good agreement for the rise time. The difference between the measured fall and rise times is due to the heat dissipation process of the device geometry [43].

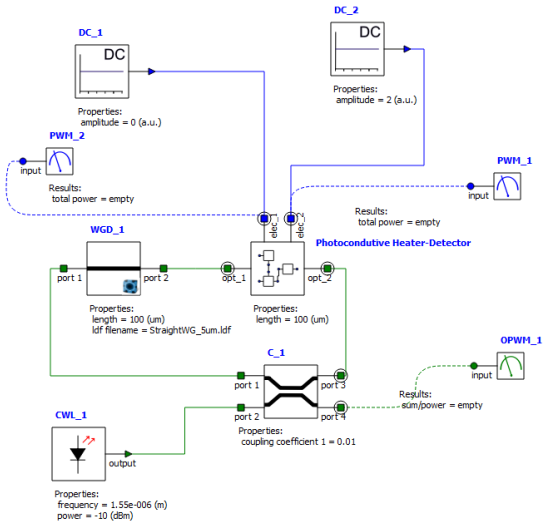

(a)

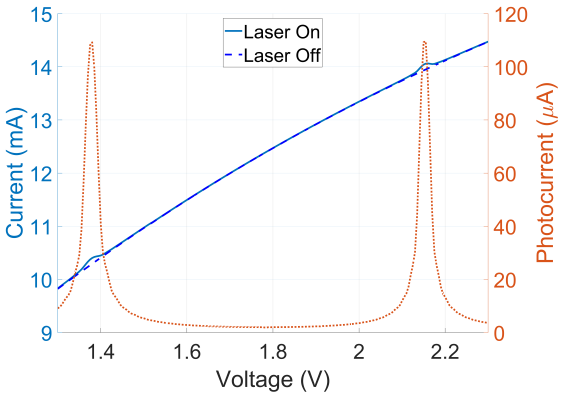

(b)

Figure 2.9: a) Test circuit with PCHD placed in a microring resonator, b) simulated sweeps of the ring resonator with and without the input laser light, with the photocurrent calculated from the subtraction of the two signals

2.5.3 In-Resonator Configuration

One of the most common integration schemes for PCHDs in circuit elements is as a portion of a microring resonator, due to the optical build-up factor which provides

a boost to the photocurrent and thus lowers the limit of detection. Here we test the PCHD model in a ring configuration to quantify the simulation performance as a detector when integrated into a resonator device. A path of 100 µm-long waveguide along with 100 µm of PCHD were connected to a directional coupler with a coupling coefficient of 0.01, then injected with a 1550 nm laser at -10 dBm as shown in Fig. 2.9a. A rib waveguide with a 500 nm width and scattering loss of 1.9 dBm/cm was used for the undoped waveguide to match the waveguide geometry of the PCHD model. Simulated results are shown in Fig. 2.9b, where the difference between the measured current from the PCHD with and without the laser on is calculated to extract the photocurrent. The spikes in photocurrent occur due to spikes in optical power when the microring is on resonance. In a detect-and-tune loop this microring resonator could be locked onto a laser of any arbitrary wavelength by tuning the PCHD voltage to maximize the measured photocurrent.

An important characterization of the PCHD as a sensing element is a comparison to existing sensors, such as germanium photodetectors (PD). We chose to compare the PCHD to a germanium PD described in [44], which was reported to have a responsivity of 1.09 A/W and a dark current of 3.5 µA. This device was selected to control for performance variability across fabrication processes, since both this device and the analyzed PCHDs were fabricated through A*STAR AMF foundry [38]. The simulation was arranged by first constructing the PCHD resonator circuit in Fig. 2.10a (in similar fashion to Fig. 2.9a), such that the PCHD had a length of 100 µm and occurpied half the total resonator length. The input port was injected with a 1550 nm laser and the ring's coupling coefficient was swept to achieve critical coupling. The laser was then swept from an injected optical power of -70 dBm to -10 dBm, and the resulting "light" current from the PCHD was measured. The dark current of the PCHD was measured and subtracted from the "light" currents to obtain the PCHD photocurrent, shown in Fig. 2.10b. To compare the germanium PD to this sweep, a similar circuit was set up based on the germanium PD resonator circuit in Fig. 2.10a. Here there is no PCHD in the resonator, resulting in a decreased waveguide loss in the cavity from the lack of dopants, specifically 0.05 dB lower loss compared to the previous circuit. The coupling coefficient of the PD tap was set such that the losses due to the introduction of the tap matched the losses from the doping loss in the PCHD circuit. The

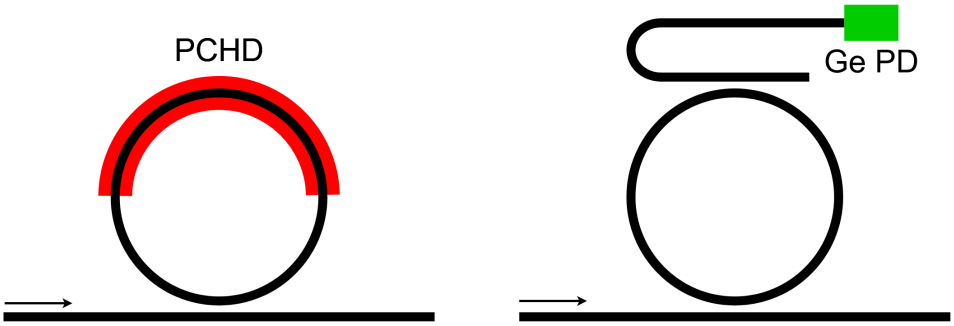

(a)

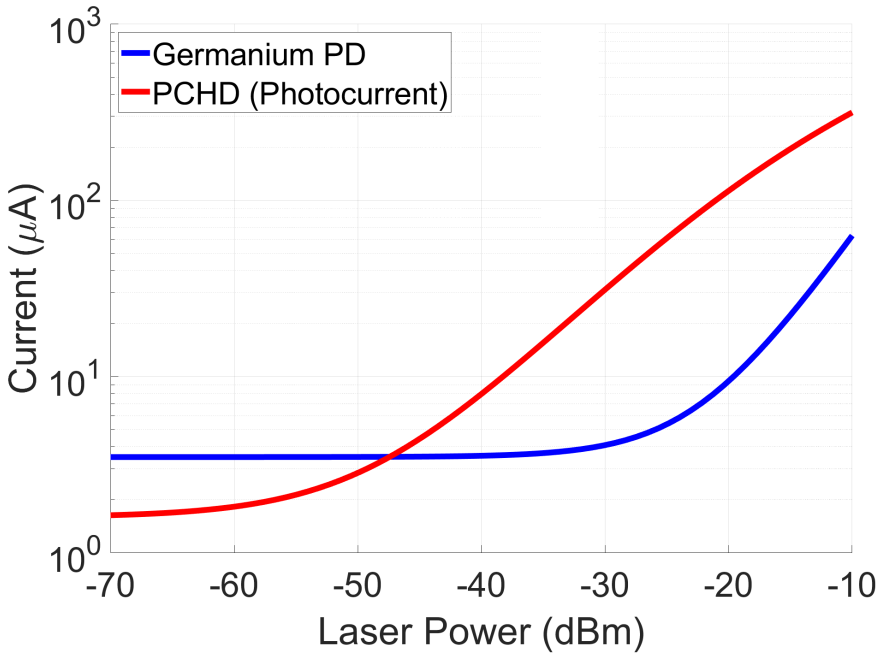

(b)

Figure 2.10: Comparison between in-resonator PCHD and equivalent germanium PD power tap for resonance photodetection, with a) device illustrations and b) simulation results. The germanium PD current is measured directly, resulting in a detection floor corresponding to the device dark current, while the PCHD photocurrent is calculated as the difference between the current with the laser on and off, with the detection floor corresponding to the device thermal noise

germanium PD was biased at -2 V and the laser was again swept from -70 dBm to -10 dBm while the current was directly measured, with the results also plotted in Fig. 2.10b. From the plot it is clear that between the two scenarios, the PCHD measures a much stronger photocurrent compared to the germanium PD, in part due to the large optical build-up in the resonator that enhances the measured photocurrent, as well as the fact that the germanium PD tap is only taking a small portion of the signal (about 1.15%). It is also apparent that for laser powers less than -30 dBm, the germanium PD is limited by its dark current, whereas PCHD is not limited by its noise floor until below approximately -60 dBm. The germanium PD would still be able to measure currents in the -60 dBm to -30 dBm range if it used a current subtraction method (if there was no other limiting detection floor in that range), but it would still produce a weaker photocurrent compared to the PCHD in this situation.

2.6 Summary

In summary, we have presented the development of a compact model for PCHD elements, based on measured results for specific n-doped devices. Model parameters come from a combination of reported values from literature and previous work, as well as through curve fits for input-dependent properties like dark current and responsivity. Simulations are presented and compared to measured results, where the model shows expected performance in a number of areas including photocurrent, noise, and modulation. A comparison between PCHD and germanium PD resonator sensing is presented, showing how PCHDs can produce much larger photocurrents under similar circuit conditions. With a strong model developed, designers will be able to characterize the performance of PCHDs in their circuits before fabrication, making the adoption of these devices in large-scale circuit more appealing and accessible.

Chapter 3

Application - Notch Filter

Notch filters are key components in integrated photonics, seeing prominent use in applications such as microwave photonics [45, 46], spectroscopy [47], biosensing [48, 49], and several others. Ring resonators are used ubiquitously in silicon photonics and are capable of top of the line performance for bandwidths, Q-factors, device footprints, and more [50]. Due to the compact device footprint of a ring resonator, tuning elements can be made very electrically efficient [30], and can be easily integrated with CMOS electronics control circuits directly [4, 51].

One of the major issues with ring resonators as filters is how sensitive their operating conditions are to fabrication deviations, which is why tunability is necessary in practice as it allows fabrication errors to be corrected [52]. Tuning is also desirable for filters in applications where circuit reconfigurability is a priority [46]. Tuning the resonant frequencies of rings can be implemented by introducing an electrical phase shifting element in the resonator, using either the TO or EO effect. However, for full spectrum tailoring, additional elements are required to change the extinction ratio, bandwidth, and free spectral range (FSR) to allow these filters to be used for various applications post-fabrication. Using a single microring with a tunable coupler offers a compact solution, but its bandwidth and extinction ratio are dependent on each other [53].

Increasingly complex notch filter architectures have been introduced to provide dynamic spectral control capabilities, including four-point coupling [54], ring loaded MZIs [46], and programmable meshes [14]. However, these designs face

a trade-off where increased spectral control requires more tuning elements and thus larger design space. For this reason, a widely tunable filter with a modest design footprint would satisfy the requirements for complex spectral reconfigurability, while not requiring designers to commit a large design space for a single filter.

Here, we demonstrate a compact tunable ring-based notch filter that allows for the independent tuning of the extinction ratio and bandwidth by controlling the power coupling to the ring and losses within the ring, along with center frequency tuning. Additionally, a two-state switching control over the free spectral range has been implemented. All tuning elements in the circuit are implemented using PCHD elements, allowing for automatic detect-and-tune controls to be configured.

3.1 Ring Resonator Theory

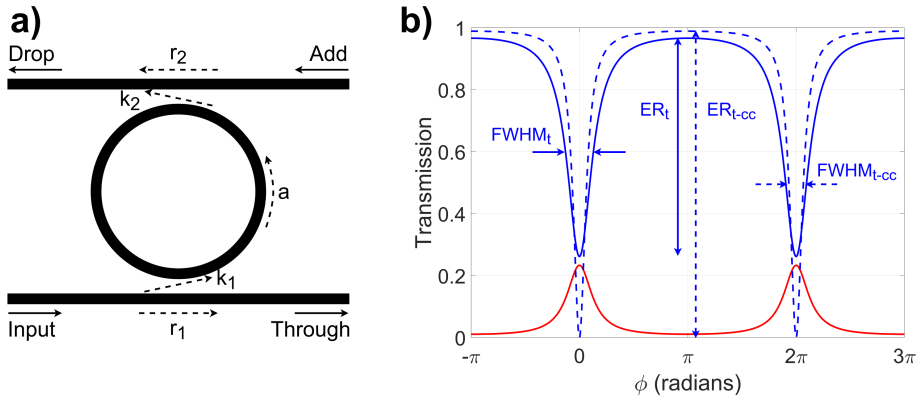

Figure 3.1: Add-drop ring resonator a) architecture and b) through port (solid blue) and drop port (red) transmission responses for $r_1 = r_2 = 0.9$ and $a = 0.8$, as well as through port (dashed blue) response for critical coupling with same coupling coefficients ($a = 1$)

Although ring resonators are very well described in literature [55], in order to fully explain the operation of the proposed filter, the general properties of add-drop ring resonators must be discussed. An add-drop ring resonator consists of a looped waveguide enclosed by two parallel bus waveguides, as shown in Fig. 3.1a. Self-

coupling r and cross-coupling k occurs between each waveguide and interior loop, where couplers are assumed to be lossless and satisfy the condition of $r^2 + k^2 = 1$. In addition to the coupling coefficients, the single-pass amplitude transmission a describes how much the field decays within the loop. The single-pass phase shift defined as $\phi = \beta L$, where β is the propagation constant and L is the round-trip length of the ring. The transmission response between the input and the through (T_t) and drop (T_d) ports can be found as [55]:

$$T_t = \frac{r_2^2 a^2 - 2r_1 r_2 a \cos\phi + r_1^2}{1 - 2r_1 r_2 a \cos\phi + (r_1 r_2 a)^2} \tag{3.1}$$

$$T_d = \frac{\left(1 - r_1^2\right)\left(1 - r_2^2\right) a}{1 - 2r_1 r_2 a \cos\phi + (r_1 r_2 a)^2} \tag{3.2}$$

3.1.1 Extinction Ratio and Bandwidth

Highlighted in Fig. 3.1b are the extinction ratio (ER) and the full width at half maximum (FWHM) for the through port, which characterize the depth and bandwidth of resonances respectively. These can both be expressed in terms of the ring parameters [55]:

$$\mathrm{ER_t} = \frac{(r_2 a + r_1)^2}{(1 + r_1 r_2 a)^2} \frac{(1 - r_1 r_2 a)^2}{(r_2 a - r_1)^2} \tag{3.3}$$

$$\mathrm{FWHM_t} = \frac{(1 - r_1 r_2 a)\,\lambda_{\mathrm{res}}^2}{\pi n_g L \sqrt{r_1 r_2 a}} \tag{3.4}$$

It is typically desirable to have ring responses with large ER for strong filtering, and small FWHM for selective filtering. From Eq. 3.3 it can be found that ER is maximized when the ring is critically coupled, or when $r_1 = r_2 a$. From Eq. 3.4 it can be found that FWHM is minimized for a value of $r_1 r_2 a$ as close to 1 as possible, but not necessarily when each term is equal. As the conditions required to meet the desired ER and FWHM are different but have two independent terms that appear in both (if a is fixed), then with careful control of coupling in and out of the ring, the bandwidth and strength of resonances in a ring spectrum can be independently adjusted.

3.2 Operating Principle and Design

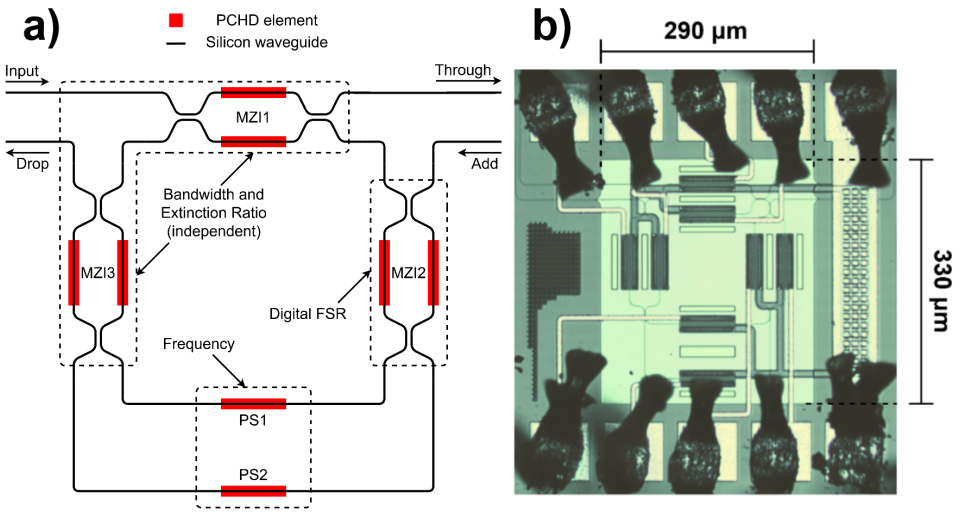

Figure 3.2: The tunable notch filter. a) Schematic illustrating the filter's spectrum tailoring elements. b) Microscope image of the fabricated device. The electrical contacts (top and bottom) were wirebonded to a PCB for the electrical control.

Fig. 3.2a shows a schematic of the tunable notch filter. The first adjustable coupler (MZI1) tunes the power coupling to the ring, whereas the third coupler (MZI3) controls the losses within the ring. As explained in Sec. 3.1, by accurately balancing the power coupling to the ring and the losses within the ring, the optical bandwidth and extinction ratio can be tuned independently of each other. The second coupler in the circuit (MZI2) acts as a switch that routes the light in the resonator to one of two paths with different lengths, resulting in an adjustable FSR. Both the short and long paths have separate phase shifters (PS1 and PS2) that allow for frequency tunability of the spectral resonances regardless of which path is selected.

The tunable couplers were implemented using balanced MZIs with PCHD elements in each branch. The couplers used in the MZIs were designed for 50/50 coupling at a wavelength of 1550 nm, but could be replaced with compact broadband couplers. The resonator cavity has a waveguide path length of approximately

725 µm and 870 µm for the PS1 and PS2 configurations respectively. The round trip path length of either configuration could be designed to provide a specific desired FSR. The device has a circuit footprint of 0.0957 mm^2, which is large in comparison to a single microring resonator, but provides dynamic spectral reconfigurability at a much smaller footprint than other widely tunable filter architectures [14, 46].

3.3 Experimental Characterization

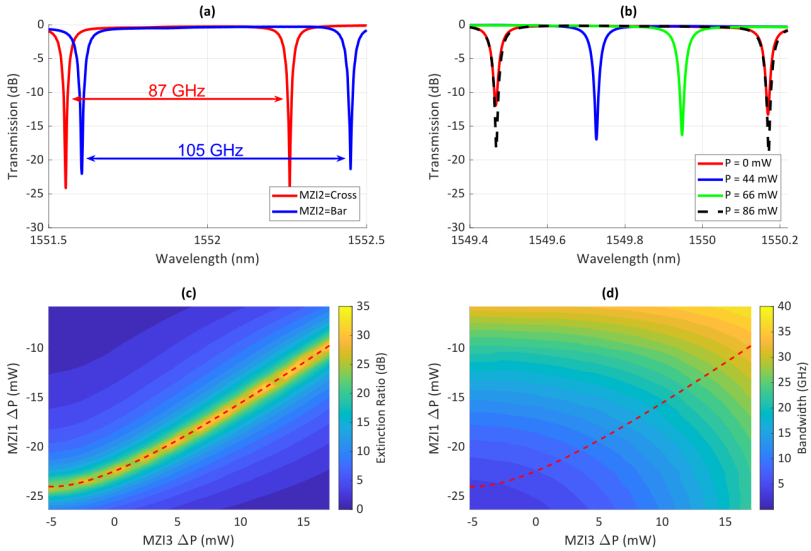

Figure 3.3: Filter through-port experimental results. a) Comparison of the FSRs for the two configurations of MZI2. b) Voltage sweep of PS2 over the full FSR. 2D sweeps over MZI1 and MZI3 for a fixed MZI2 showing c) extinction ratio and d) bandwidth of the resonance at 1549.45 nm in b) (for no electrical power applied to PS2)

The device was fabricated at the A*STAR AMF foundry in Singapore, using 193 nm deep-UV lithography [38]. An optical microscope image of the device is shown in Fig. 3.2b. Electrical connections to the device were made via wire-bonding the on-chip electrical contacts to a custom-designed PCB. The electrical control of the phase shifters was implemented using a PXIe multi-channel voltage

source driven by Python. Surface grating couplers were used to couple light from a tunable laser (Agilent 81600B) to the input of the device and from the device's through port to a photodetector (Agilent 81635A).

For characterization purposes, MZI2 was set to the cross-state for all reported measurements, i.e., the circuit was configured to the longer path length option (smaller FSR). All of the MZIs were operated in a push-pull configuration, such that the total electrical power applied to each pair of MZI phase shifters was constant, where 42 mW was found to be sufficient to give tunability over the entire FSR of the MZI. The push-pull configuration ensured that the overall phase was constant and thus the resonant frequency was not shifted due to tuning of any element other than PS1 or PS2. All reported measurements were extracted from a parameter sweep of the relevant tuning elements.

Fig. 3.3a shows how the FSR of the filter can be adjusted by setting MZI2 to either the cross or bar state, with measured FSRs of 0.70 nm and 0.84 nm, respectively, at the through port shown in Fig. 3.2a. Fig. 3.3b shows the shift of resonances over a full FSR, achieved with an applied electrical power of 86 mW. Figures 3.3c and 3.3d show the extinction ratio and bandwidth measured from the through port response over a 2D sweep of MZI1 and MZI3, where the x- and y-axis labels indicate the electrical heater power difference between the two arms of each MZI in the push-pull configuration. The dotted red line in Fig. 3.3c is overlaid in Fig. 3.3d, showing that at the maximum extinction ratio (approximately 30 dB) the filter covers a tunable bandwidth range from 5 to 34 GHz.

3.4 Detect and Tune

Sec. 3.3 reported experimental results that demonstrated spectral reconfigurability through wide parameter space sweeps. Here we make use of the PCHD compact model from Chp. 2 to highlight the ability of PCHD elements to implement detect-and-tune feedback loops that can automatically configure the circuit without the need for sweeping and mapping the parameter space.

A model for the circuit was built in INTERCONNECT, shown in Fig. 3.4. Each PCHD element was connected to a source measure unit (SMU) controlled via script to allow for sweeps over voltage while reading current from each device

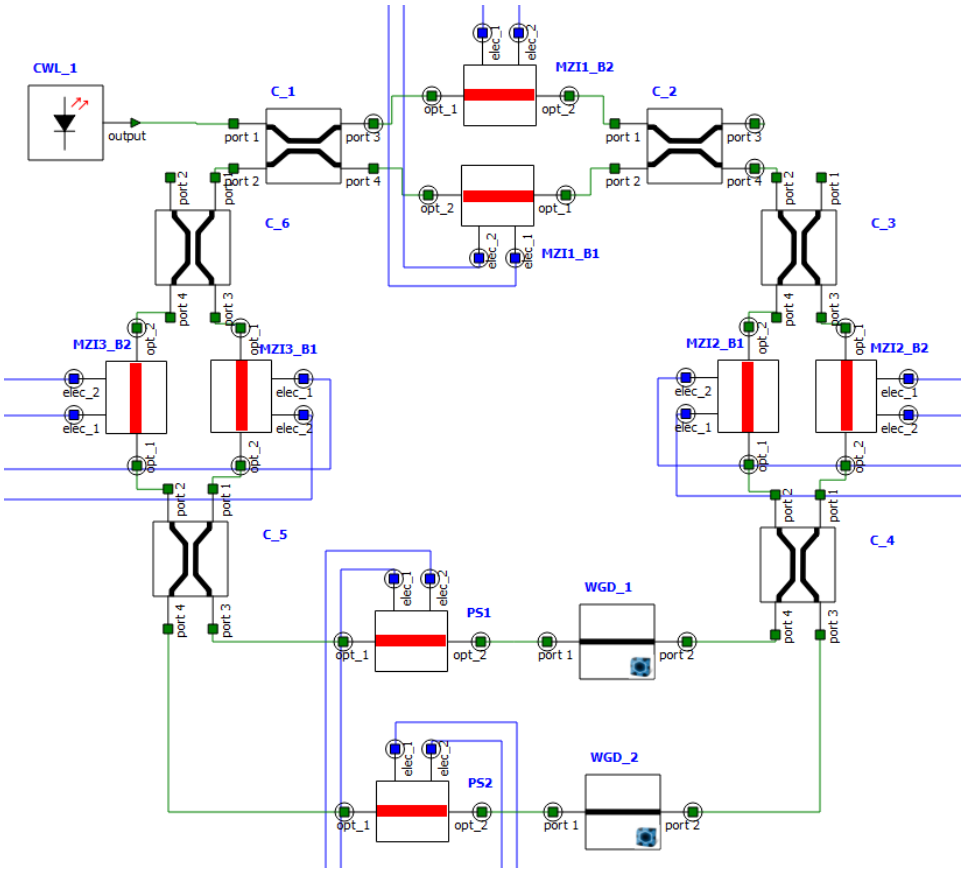

Figure 3.4: The tunable notch filter INTERCONNECT model

in the circuit. All of the MZIs were operated in a push-pull configuration such that the total electrical power applied to each pair of MZI phase shifters was constant, ensuring that the overall phase was constant while sweeping and thus the resonant frequency was not shifted due to tuning of any element other than PS1 or PS2. An electrical bias of 15 mW between the two branches was found to be sufficient to give tunability over the entire FSR of a single MZI coupler. Photocurrents from the PCHD elements were obtained by performing a subtraction between the measured current while the laser was on and off.

As an example for how this circuit could be automatically configured, we have chosen to demonstrate how the resonant wavelength can be set to a wavelength

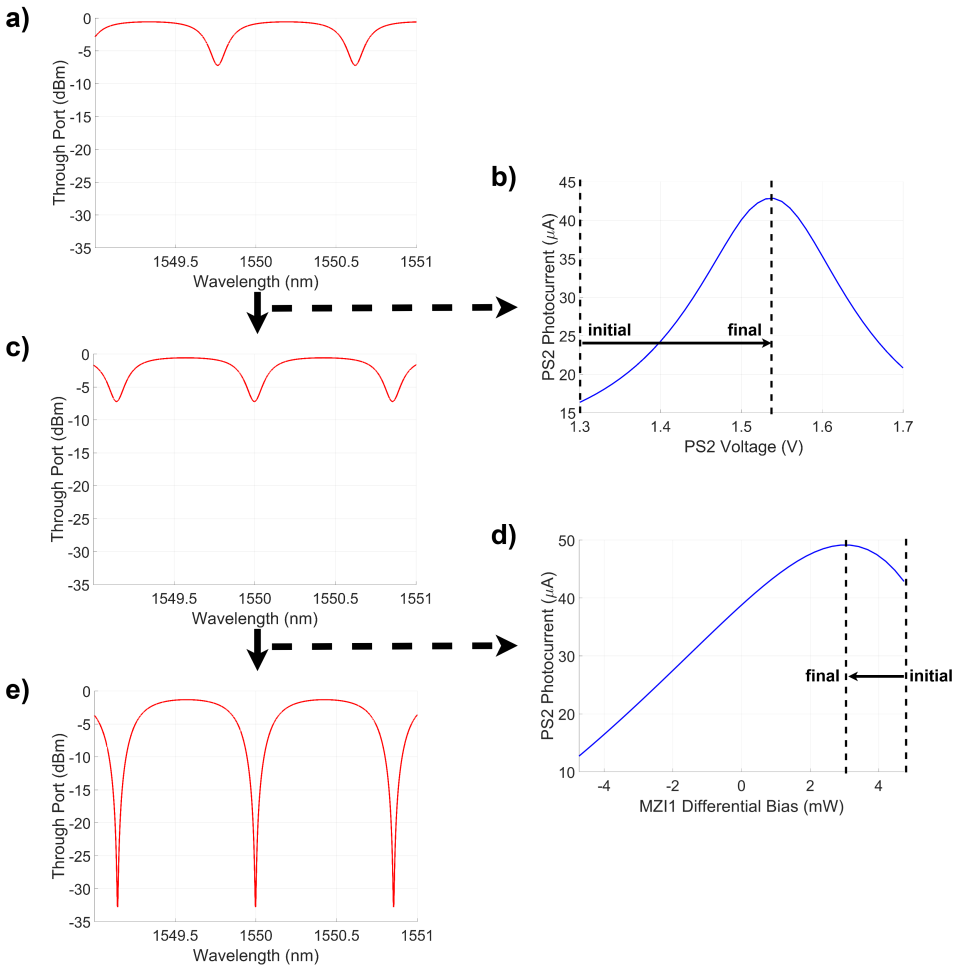

Figure 3.5: Filter tuning process used to align filter resonance wavelength to 1550 nm and maximize the extinction ratio

of 1550 nm, and the extinction ratio maximized. To demonstrate this, the circuit model was initialized with a random set of biases (with MZI2 fixed to route all light through PS2), which produced the wavelength response shown in Fig. 3.5a. In practice this response would not be suitable for applications using a 1550 nm laser as the resonance is not centered at 1550 nm and the extinction ratio is poor ($<$10 dB). To tune the resonance wavelength we inject light in the input port at

1550 nm, and sweep PS2 while measuring its photocurrent, as shown in 3.5b. The bias that produces maximum photocurrent corresponds to the PS2 bias required to align the filter resonance at a wavelength of exactly 1550 nm, as shown in 3.5c. Next, to simply maximize the extinction ratio of the filter either MZI1 or MZI3 needs to be tuned to reach the critical coupling condition by matching the losses of the other coupler (note that this does not act to minimize the filter bandwidth, which would require additional tuning steps). MZI1 was swept differentially (where a positive difference indicates a larger electrical bias on the outer MZI branch) while the photocurrent at PS2 was measured. The location of maximum photocurrent is shown in 3.5d, which corresponds to the MZI1 bias required to achieve maximum extinction ratio, as shown in 3.5e.

3.5 Summary

In summary, we demonstrated a tunable ring-based notch filter with independent bandwidth and extinction ratio control, as well as two FSR configurations. Measured results show the filter is capable of bandwidths between 5 to 34 GHz while maintaining an extinction ratio in of approximately 30 dB. Simulated results of the circuit's automated tuning capabilities are presented to highlight the use of the PCHD compact model in a circuit application. This type of device would be useful in a number of fields like microwave photonics, where a widely reconfigurable filter could be used to provide the functionality of several different discrete filters.

Chapter 4

Application - Biosensor

Medical diagnostic testing has taken renewed importance in light of the COVID-19 epidemic. As governments struggle to ensure public safety without imposing restrictions that cause economic harm, fast and accurate COVID-19 testing on a massive scale is necessary for informed decision making. A report published on May 1, 2020 [56] looking at a collection of COVID-19 nucleic acid diagnostic tests found the lowest cost per test (excluding labour and equipment) to be $3.5 USD. With medical professionals proposing universal weekly testing protocols as an exit strategy to the pandemic [57], Canada would require on the order of 2.7 million tests (or at least $9.45 million USD) per day at a compliance rate of only 50%. This clearly motivates the need for high-volume, low-cost diagnostic kit production for COVID-19 detection.

Silicon photonics has proven to be a robust platform for developing optical sensors, thanks in part to the high index contrast that permits extreme miniaturization and integration density, compatibility with CMOS electronics, and its scaleable, cost-effective manufacturing process. A variety of architectures have been proposed and validated, including ring [49, 51] and interferometer [48, 58, 59] based sensors. Most existing integrated photonic biosensors rely on the use of a sweepable wavelength source [48, 49], in part due to their abundance in research settings. Unfortunately, sweepable lasers are expensive and bulky, preventing deployment in point-of-care settings where such a sensor could more quickly provide health care specialists with relevant diagnostic information. On the other hand, single wave-

length lasers are much cheaper and smaller than their sweepable counterparts. A sensor architecture that could provide the same or improved levels of sensitivity as existing architectures while driving down cost and size by using single wavelength lasers would provide a tangible benefit to healthcare workers and recipients.

Here we propose a novel biosensor architecture that provides detection limits on the same order as sweepable wavelength sensors, but instead relies on the use of a fixed-wavelength laser. The design makes use of an in-resonator PCHD element that provides a method for electrically detecting resonance shifts due to changes in the sensor medium, allowing a much smaller form-factor for total system integration.

4.1 Sensor Architecture

A traditional ring-based biosensor is shown in Fig. 4.1a, where the sensing region is exposed to a fluidic sample. As the sample binds to the resonator (surface sensing) or the sample contents change with time (bulk sensing), the resonant condition of the system changes. This shift is measured by injecting the resonator with light at a large number of wavelengths and observing how the power spectrum changes with time.

The newly proposed sensor architecture shown in Fig. 4.1b restricts the sensing region to a portion of the cavity and allocates an area within the resonator to place a PCHD element. The benefit of placing the PCHD within the resonator rather than at the device through port is that the optical build-up that occurs within the resonator acts to increase the detected photocurrent and thus increase the electrical detection limit. For a single wavelength injected into the resonator system, an electrical sweep of the PCHD while measuring photocurrent provides a spectrum that mirrors the wavelength-swept sensor, but with photocurrent peaks where troughs occur in wavelength, as the electrical signal is measured within the cavity instead of the through port.

4.2 Performance Metrics

Some of the most important metrics of characterizing the performance of a sensor are the bulk sensitivity (S_b), surface sensitivity (S_s), and the intrinsic limit of

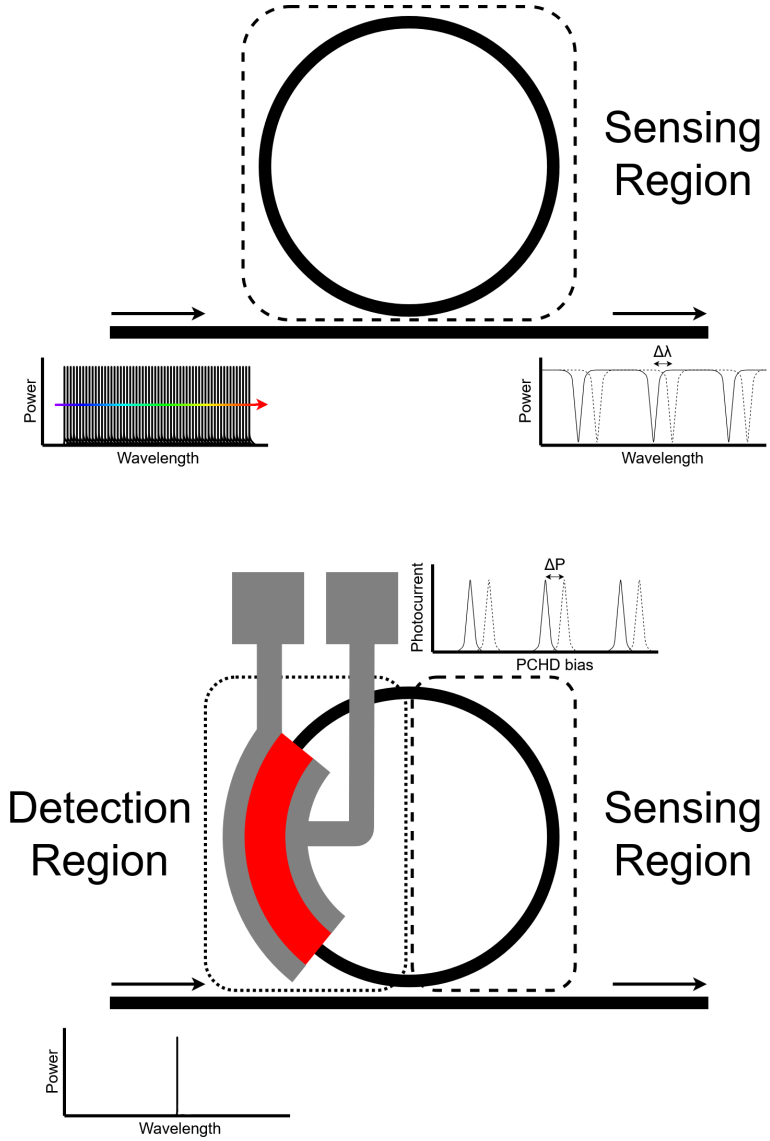

Figure 4.1: Biosensor architecture for a) a wavelength-sweepable sensor and b) a single wavelength, PCHD-sweepable sensor

detection (*iLoD*). While surface sensitivity is a more valuable measure for target molecule detection [60], it typically also has a lower *iLoD*, the reason for which we will only analyze the bulk sensitivity.

Bulk sensitivity is defined as the change in resonance wavelength ($\Delta\lambda_{res}$) due to a change in the surrounding refractive index of the device (Δn_{clad}) [60]:

$$S_b = \frac{\Delta\lambda_{res}}{\Delta n_{clad}} = \frac{\lambda_{res}}{n_g}\left(\frac{\partial n_{\text{eff}}}{\partial n_{\text{clad}}}\right) = \frac{\lambda_{res}\cdot S_{wg-frac}}{n_g} = \frac{\lambda_{res}\cdot S_{wg}}{n_g}\cdot ff \tag{4.1}$$

where n_g is the group index of the resonator and S_{wg} is waveguide mode sensitivity. For resonator sensors where only a portion of the resonator path length acts in a sensing capacity, like in Fig. 4.1b, the waveguide mode sensitivity in Eq. 4.1 should be scaled by the percentage of the resonator path that is used for sensing, known as the fill factor ff. This quantity is called the fractional sensitivity $S_{wg-frac} = S_{wg}\cdot ff$. The group index n_g in Eq. 4.1 refers to the effective refractive index of the entire resonator, which can be extracted via the FSR as

$$n_g = \frac{\lambda^2}{L\cdot FSR} \tag{4.2}$$

where λ is the resonance wavelength and L is the length of the entire resonator.

The quality factor is used as a measure of how long energy stays within a resonator, which can give a sense as to how the losses in the system affect the performance. Sometimes approximated by the ratio of the resonant wavelength to the FWHM, the upper limit for Q is formally expressed as [55]:

$$Q = \frac{2\pi\cdot n_g\cdot 4.34}{\lambda_{res}\cdot\alpha_{(\text{dB/m})}} \tag{4.3}$$

where $\alpha_{(\text{dB/m})}$ is the propagation loss within the resonator in decibels per metre.

Rather than actually try to detect the smallest possible refractive index change which would potentially end up being limited by the noise levels of instrumentation or environmental factors, the *iLoD* provides a robust calculation for the minimum detectable change in resonant wavelength due to a change in refractive index [60]:

$$iLoD = \frac{\lambda_{res}}{Q\cdot S} \tag{4.4}$$

Finally, to give a sense of how well resolved the signal will be rather than look at the absolute measured photocurrent for a detector, it is useful to compare

the measured resonance photocurrent I_{res} to the dominant limiting factor. In some scenarios the best metric for this would be the signal-to-noise ratio (SNR), but since the measured signals in this application can be very large (hundreds of μA) in comparison to the device noise (hundreds of nA), it is instead better to compare the off resonance photocurrent I_{off} of the circuit via the extinction ratio ER:

$$ER = \frac{I_{res}}{I_{off}} \tag{4.5}$$

4.3 Circuit Design

The sensor layout shown in Fig. 4.4 was selected for the optical biosensor design to balance an optimized performance with the physical constraints of integrating optical, electrical, and fluidic interfaces. The primary concern was the large area needed to place a microfluidic gasket on the chip surface, while avoiding fluidic contact with the electrical and optical ports. This design constraint required the use of a large resonator cavity that contained the sensing region at one end, and the electrical and optical connections at the other, with a separation between the two regions greater than 1 mm.

Due to the large number of waveguides and transitions in the signal path, as well as the wafer variability over the large area the circuit occupies, the uncertainty on the exact losses in the resonator necessitated the use of a tunable coupler for the cavity that could be optimized on a per-circuit basis. Standard TE strip waveguides were used for compact routing in the circuit, while 3 μm wide multi-mode waveguides were used for long distance routing due to their lower propagation loss, attributed to strong mode confinement and less scattering from surface roughness on the waveguide sidewalls. The sensing region of the device contains a number of sections of straight subwavelength grating (SWG) waveguides, which have been demonstrated to have waveguide mode sensitivities much higher than that of strip TE or TM waveguide sensors [48]. The oxide cladding above the sensing region is selectively etched to allow the biological solutions to come in direct contact with the sensor, while the rest of the chip maintains its protective cladding.

Part of the design process was to investigate the use of different sensing waveguides, focusing primarily on the differences between SWG and SWG-assist (or

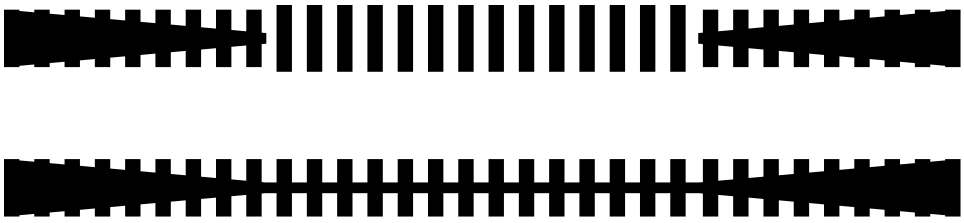

Figure 4.2: Difference between SWG (top) and SWG-assist/fishbone (bottom) waveguides, including strip-SWG taper transitions

fishbone) waveguides shown in Fig. 4.2. SWG waveguides have been demonstrated as excellent waveguides for sensing applications [2, 48], but it is currently a challenge for manufacturers to produce silicon structures in oxide-open windows with small feature sizes, as they can end up getting their base under-etched and end up lifting from the buried oxide layer. As an alternative that still has higher sensitivity compared to strip waveguide but is less of an issue to fabricate, the fish bone structure is a good candidate as it maintains the waveguide as a homogeneous piece of silicon which is less likely to be etched away in fabrication. Additionally, the continuity of the taper strip throughout the fishbone waveguide keeps the effective index transition continuous throughout the structure, thus avoiding additional unwanted losses and reflections from the taper interface. For pure SWG waveguide transitions, the taper end widths need to be specifically designed to avoid an index mismatch.

Another major variation we considered for our designs was circuit operation in the C-band and the O-band. The primary motivation of this sensor architecture is to create a fully-contained sensor package that does not require the use of external equipment. Compact single-wavelength lasers can be purchased from a number of vendors for a wide range of optical bands, but lasers in the C-band are more difficult to manufacture and thus more expensive compared to those in the O-band [61], which is an important factor when considering the desire for low-cost, high volume production of such sensors. The other consideration between the two bands is that the absorption of water is about ten times greater in the C-band [3, 62] as shown in Fig. 4.3, meaning O-band sensors of the same circuit architecture could potentially have better performance. We still chose to design several C-band

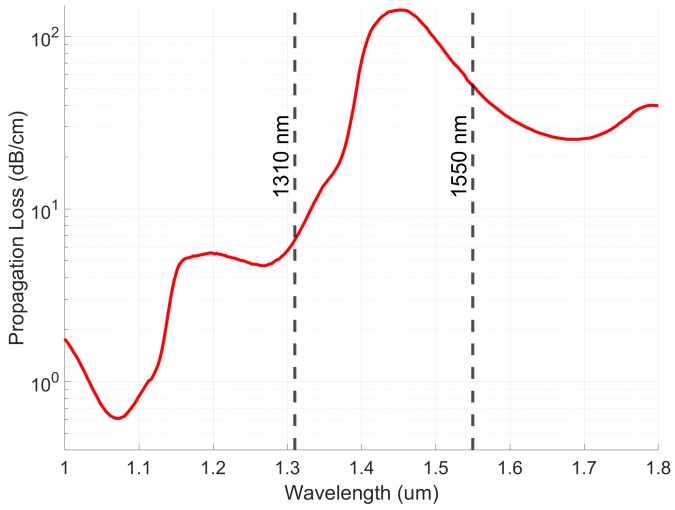

Figure 4.3: Propagation loss of water as a function of wavelength [3]

variants as much of our test equipment is made for the C-band, including things like sweepable lasers and detectors that aren't necessary for the targeted operation, but can still be used for broader circuit characterization.

One of the most important parameters for modeling the sensor's performance is the SWG propagation loss for 1550 and 1310 nm. Unfortunately there are no reported measured values for propagation loss of SWG waveguides with a water cladding for devices in Applied Nanotools Inc.'s process, where our designs are manufactured. Based on previous work of similar structures [2], our best guess for material absorption and scattering loss at 1550 nm for this fabrication process are 25 dB/cm and 5 dB/cm respectively, for a total propagation loss of 30 dB/cm. At a wavelength of 1310 nm the scattering loss is expected to be similar, while the material absorption should be approximately ten times smaller, for an estimate of 2.5 dB/cm, and a total propagation loss estimate of 7.5 dB/cm. All SWG loss values are summarized in Tab. 4.1.

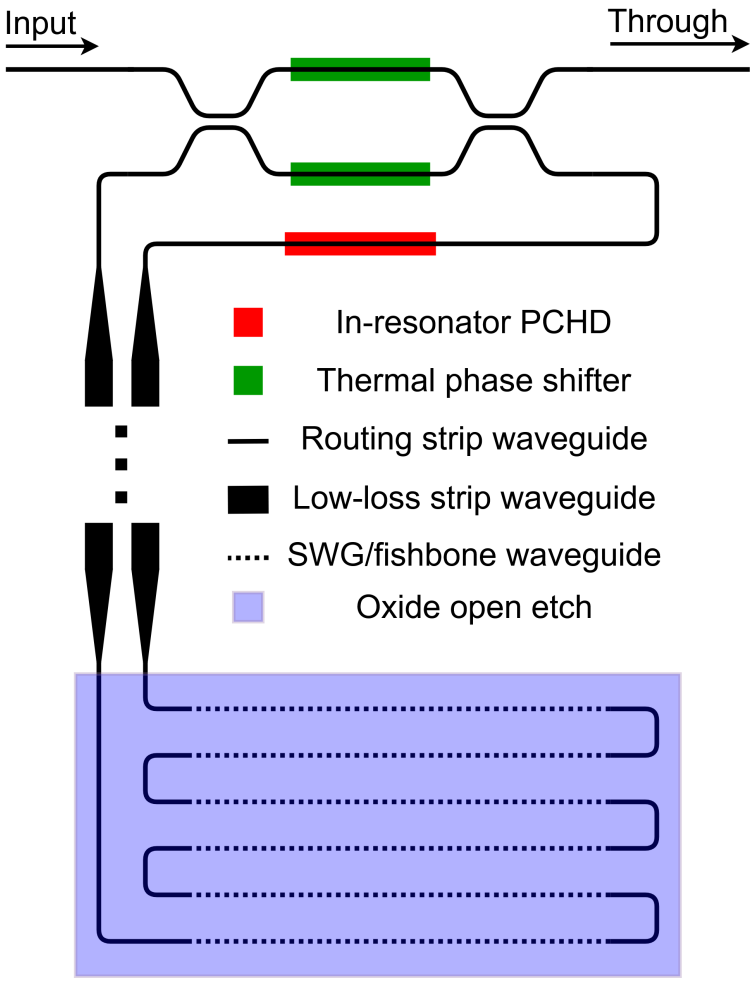

Figure 4.4: Proposed biosensor circuit layout, including a balanced MZI for tunable coupling to the resonator

4.4 Simulation Results

To assess the circuit performance in terms of sensitivity and detection limits, a full electro-optic model of the circuit was implemented in INTERCONNECT. Strip and rib waveguides were simulated using 2D Lumerical MODE simulations to extract compact models for effective index, group index, and loss, for both curved and straight variants. SWG waveguide models were extracted through 2D MODE

Table 4.1: SWG propagation loss estimates based on [2]

Wavelength (nm)	1550	1310
SWG material absorption loss (dB/cm)	25	2.5
SWG scattering loss (dB/cm)	5	5
SWG total loss (dB/cm)	30	7.5

simulations as well, using the effective index method to approximate the SWG waveguide as a strip waveguide with a water cladding. To accurately capture the waveguide mode sensitivity $S_{wg} = \delta n_{eff}/\delta n_{clad}$, 3D FDTD simulations were performed for the SWG and fish bone waveguide sensors for cladding refractive indices from 1.33 to 1.34, chosen to be within the range of refractive indices for a water based-solution. These simulations found no meaningful difference in S_{wg} between the SWG and fishbone structures, so all circuit simulation results for SWG sensors are assumed valid for fishbone based sensors as well. All tapers in the circuit were simplified using variable attenuators set to values from literature or previous simulations, shown in Tab. 4.2. The PCHD detector in the circuit was implemented using the model developed in Chp. 2. Since no compact model in INTERCONNECT was available for the high-efficiency TO heaters used in the design, PCHD elements were substituted for use as phase shifters. The broadband 3 dB couplers used in the layout were approximated by a point coupler with a coupling coefficient of 0.5, with the coupler length shifted to the waveguides within the MZI to maintain a path length representative of the designed circuit.

Tab. 4.2 provides the circuit parameters, extracted values, and calculated quantities for two circuit variants. All simulations presented in this chapter used optical sources with a power of 0 dBm directly at the input port of the device in Fig. 4.4. For each simulation, the tunable MZI coupler is swept and calibrated by maximizing the extinction ratio to ensure critical coupling to the ring. Calculation of *iLoD* from Eq. 4.4 for a given circuit configuration requires determining both Q and S. Q can be extracted directly through the use of an optical network analyzer element in INTERCONNECT. S is calculated by sweeping refractive index exposed to the

Table 4.2: Circuit parameters and performance analysis for two circuit variants in INTERCONNECT, where reported taper losses are for individual components, and the total SWG waveguide length L_{SWG} is discretized into 120 µm sections and looped back and forth as shown in Fig. 4.4

	$\lambda = 1550\,\text{nm}$, $L_{SWG} = 240\,\mu\text{m}$	$\lambda = 1310\,\text{nm}$, $L_{SWG} = 2400\,\mu\text{m}$
Circuit parameters		
Narrow-to-wide taper loss (dB) [63]	0.002	0.002
Strip-to-rib taper loss (dB) [64]	0.012	0.012
SWG-to-strip taper loss (dB)	0.1	0.1
SWG S_{wg}	0.7830	0.7872
Total resonator length (mm)	3.654	6.277
From Interconnect		
FSR (pm)	241.0	75.7
Q (1e4)	5.616	4.756
I_{res} (µA)	277.2	81.4
Calculated		
Sensor fill factor	0.0657	0.3823
SWG $S_{wg-frac}$	0.0514	0.3009
n_g [Eq. 4.2]	2.73	3.61
S_b (nm/RIU) [Eq. 4.1]	29.2	109.3
$iLoD$ (RIU) [Eq. 4.4]	9.45e-4	2.52e-4
ER [Eq. 4.5]	8.35	1.83

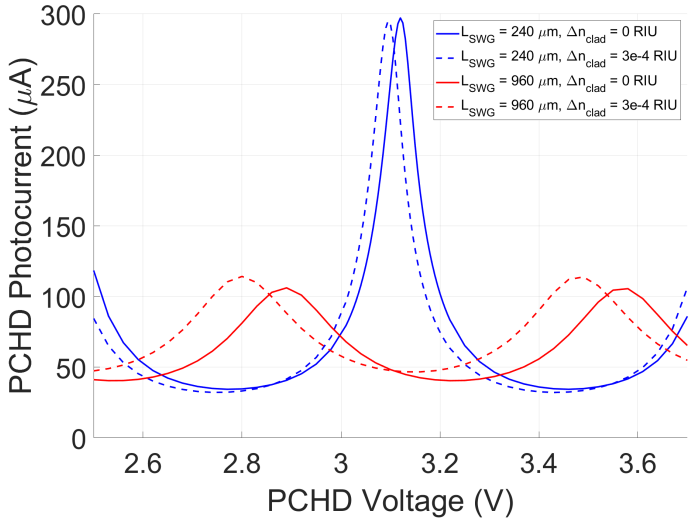

Figure 4.5: PCHD voltage vs. photocurrent for two sensing region lengths, and two different n_{clad}, demonstrating how a longer sensing region produces weaker photocurrent peaks but strong sensitivity to environmental changes. The difference between photocurrent peaks is 25 mV and 90 mV for $L_{SWG} = 240\,\mu m$ and $L_{SWG} = 960\,\mu m$ respectively. Results are for C-band sensors.

sensor and measuring the wavelength shift of the resonances. To extract the ER of the electrical signal, the photocurrent of the circuit is calculated at resonance by taking the difference of the PCHD current with the laser on and off, which is then divided by the off resonance photocurrent.

A critical component of this sensor architecture is the sensing region length, due to the effect it has on cavity losses as well as environmental sensitivity. As shown in Fig. 4.5, a sensor with a long sensing region will be more sensitive to changes in the cladding refractive index, but at the cost of a weaker photocurrent signal. This trade-off is an important parameter for the design and operation of these sensors, which is assessed in Fig. 4.6. Fig. 4.6a shows how both S and Q are affected by changes to the sensing length in this design. As the proportion of the ring cavity that is filled with sensor increases, the sensitivity increases asymptotically to the fully filled sensor sensitivity value ($ff = 1$). Conversely, the quality

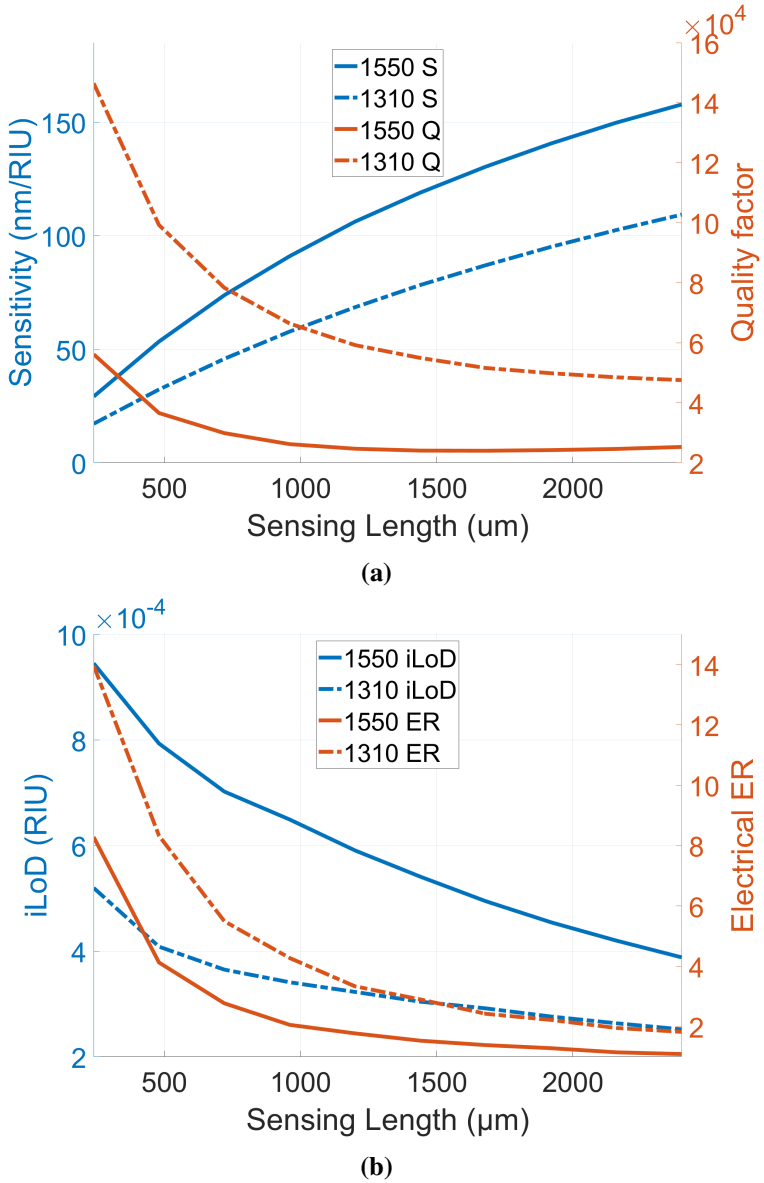

Figure 4.6: Simulation results of the 1310 nm and 1550 nm sensor circuits for a) Q and S, and b) iLoD and ER

factor decreases as the length increases and losses within the ring increase. Fig. 4.6b shows the trade-off between intrinsic limit of detection *iLoD* and electrical

ER, where a low *iLoD* and a high *ER* are considered desirable. As shown, the *iLoD* continues to improve as the sensor length increases, but at the cost of a worsened *ER*. While is unclear as to what length is optimal for overall system performance, it is clear that the 1310 nm design consistently sees better performance in terms of *iLoD* and *ER*, due largely to the lower optical losses occurring within the sensing region.

Although the architecture and operation of this sensor is quite different compared to wavelength-swept sensors, it is important to compare these results to those of other integrated biosensors to get a sense of the relative performance of this device. A recent multi-box SWG ring resonator sensor operating in the C-band [60] reported a measured bulk sensitivity S of 580 nm/RIU, quality factor Q of 2600, and bulk *iLoD* of 1.02×10^{-3} RIU. The high sensitivity of this device compared to our simulations in Fig. 4.6a comes in part due to the multi-box structure used, which creates an optical mode that propagates more in the cladding compared to SWG resonators and thus reacts more strongly to environmental changes. Another aspect which increases the sensitivity is the use of the entire resonant cavity for sensing rather than just a portion of it, as shown in Eq. 4.1. However, greater losses are present in the multi-box sensor due to the loosely confined optical mode as well as higher scattering losses from increased side-wall roughness exposure, resulting in a much lower quality factor compared to our devices. Since *iLoD* is dependent on both Q and S as shown in Eq. 4.4, even though the multi-box sensor has a superior sensitivity, the overall limit of the sensor is not as good as what can be achieved with our device in simulation. As our architecture also relies on a strong optical power for a larger measurable photocurrent, our sensor will see overall better performance for lower S and higher Q, even if the *iLoD* remains constant. Therefore, minimizing the cavity losses is a critical aspect of the design of the proposed sensor, even if it comes at the cost of reduced sensitivity.

4.5 Summary

In summary, we have demonstrated a new single-wavelength sensor architecture that aims to significantly lower the operational and fabrication costs associated with integrated photonic biosensors. Performance metrics including *iLoD* and *ER* were

introduced to provide a quantitative method of assessing the sensor performance. The pros and cons of several design variants were discussed, including the use of SWG and fishbone waveguides for the sensing medium, as well as the choice of C-band or O-band operation. Simulations of the full sensor circuit were presented and discussed, including an analysis of how changing the length of the sensing region presents a performance trade-off between the biological sensitivity and the measured electrical response of the device.

Chapter 5

Conclusion

In conclusion, we have demonstrated an empirical compact model for PCHD elements and highlighted the use of PCHD elements in a widely tunable notch filter, as well as in a novel single-wavelength biosensor architecture. The major contributions of this thesis include:

- Design and implementation of a compact model structure for an n-doped PCHD element, including a full comparison of the model to measured optical and electrical results for validation. As there are no other models available for PCHD devices, the work presented here will enable designers to characterize the performance PCHD devices before fabrication, making them more likely to adopt the use of these devices over discrete phase shifter or detector elements.

- Measurement of a widely tunable filter design, with independent bandwidth, extinction ratio, FSR, and wavelength resonance tuning demonstrated. Additionally, simulated results were presented to demonstrate how the filter can be configured to create automated feedback control loops, highlighting how circuit designers can make use of the PCHD model to develop and test feedback control loops in simulation.

- Design of a novel biosensor architecture implementation, backed by quantitative simulation results showing the relationship between sensing region length and sensor performance. Since this sensor architecture forgoes the

need for a sweepable laser source, the cost of manufacturing and operating these sensors is driven significantly down, making them more viable for large-scale use in diagnostic detection of biological targets of interest such as COVID-19.

5.1 Future Work

The intent of this thesis is to demonstrate the utility of PCHD devices in scaleable circuits, and how a compact model for these devices enables designers to better estimate the performance of their circuits before fabrication. To this end, there is still much room for improvement in both the modeling of these components on the device and circuit level, and there are many future research directions that the proposed filter and sensor applications could be taken.

5.1.1 Photoconductive Heater-Detector Model

While the model proposed here stands up well to the measured results it is built upon, there is much room for improvement. Firstly, it would be beneficial to develop a model based on physical properties rather than measured results. While it may not be as succinct as the model we developed, a physical model would provide more accurate performance estimates for device operation outside of the measured conditions we assessed, and would provide a more convincing argument to users that the model they are using will stand up in their use cases, including for different PCHD geometries, doping types, doping profiles, and fabrication processes. The primary constraint on this approach is the difficulty in incorporating the appearance of defect states in the waveguide core from the doping process, as Lumerical's simulation tools do not currently have an obvious approach available to users for integrating fabrication effects into device properties.

The model would also benefit from an assessment of how the doping profile (n++ separation, doping density) affects the electrical and optical properties of the device. This would likely necessitate the inclusion of additional elements to the model structure, but it would provide an additional dimension of flexibility for designers to tailor the PCHD for their specific situational requirements. Along with this, the model would also benefit from both simulated and measured validation

that the PCHD would operate similarly in the O-band, which has yet to be demonstrated.

5.1.2 Notch Filter

One of the main arguments in favour our filter design against current alternatives is the design footprint required is much smaller than some of the alternatives [14, 46]. To this effect, further development of this filter architecture could focus on smaller designs, with room for improvement available through shorter PCHD elements, or rearrangement of the circuit to avoid dead space in the center of the circuit. Other than the footprint, one of the main attractions of the filter is its utility in broad spectral reconfigurability. Further utility could be derived from this circuit architecture if it were able to be used as more than just a filter. For example, similar resonator schemes have been used to calculate fabrication-dependent parameters like propagation loss [65].

Another important area for further work would be to validate the simulated detect-and-tune control loops through circuit measurements. This would substantiate the design as a practical solution, and open up room for further improvements to the proposed control schemes, including looking at developing and implementing CMOS electronics to drive the circuit rather than the Python driven SMUs that were used. Finally, it would be interesting to investigate developing more complicated feedback loops that use two or more PCHD sensors at a time to simultaneously control more than one figure of merit, such as extinction ratio and bandwidth.

5.1.3 Biosensor

As the content presented here only covered the design and simulation results of this biosensor architecture, there is much experimental work left including demonstration of the device as a viable alternative to conventional photonic biosensors. Since the major benefit of this architecture is the potential for an extremely low cost diagnostic solution, there is much room to explore packaging options in terms of optimizing cost to performance.

As explained before, the main trade-off of this architecture with increasing sensor length is the increase in sensitivity and decrease in photocurrent signal. Since a

more sensitive sensor is desired, an important analysis of this architecture would be to determine how long of a sensor would be viable before the photocurrent signal can no longer be resolved, due to a decreasing *ER* in the measured response. This analysis could be facilitated by the development of a new performance metric that factors in both the *iLod* and *ER*, such that the need for a sensitive device but also a strong electrical response are simultaneously factored in. Additionally, an analysis of the system limit of detection (*sLoD*) would provide a better understanding for how resolvable the electrical signal is for some given operating conditions for measurement of the circuit.

A critical part of the experimental sensor operation will be to determine how to control the circuit's electrical tuning elements to maintain both critical coupling and resonance alignment to the laser's wavelength at all times, without assistance from any wavelength sweeps. Integration of additional detectors might help with this, and CMOS controls can be implemented to facilitate the operation once a suitable control scheme is determined. It will be important to ensure sufficiently fast control operation (on the order of kHz) to ensure that any abrupt changes in the sensing medium are detected and accounted for.

Bibliography

[1] Connor Mosquera, Hossam Shoman, and Lukas Chrostowski. A widely tunable notch filter on soi platform. *IEEE Photonics Conference*, 2020. → page vi

[2] Enxiao Luan. *Improving the performance of silicon photonic optical resonator-based sensors for biomedical applications*. PhD thesis, University of British Columbia, 2020. → pages x, 36, 37, 39

[3] Linhong Kou, Daniel Labrie, and Petr Chylek. Refractive indices of water and ice in the 0.65-to 2.5-μm spectral range. *Applied optics*, 32(19): 3531–3540, 1993. → pages xiii, 36, 37

[4] Adil Masood, Marianna Pantouvaki, Danny Goossens, Guy Lepage, Peter Verheyen, Joris Van Campenhout, Philippe Absil, Dries Van Thourhout, and Wim Bogaerts. Fabrication and characterization of cmos-compatible integrated tungsten heaters for thermo-optic tuning in silicon photonics devices. *Optical Materials Express*, 4(7):1383–1388, 2014. → pages 1, 3, 22

[5] Lukas Chrostowski, Hossam Shoman, Mustafa Hammood, Han Yun, Jaspreet Jhoja, Enxiao Luan, Stephen Lin, Ajay Mistry, Donald Witt, Nicolas AF Jaeger, et al. Silicon photonic circuit design using rapid prototyping foundry process design kits. *IEEE Journal of Selected Topics in Quantum Electronics*, 25(5):1–26, 2019. → pages 1, 3, 8

[6] David E Hagan, Mengyuan Ye, Peng Wang, John C Cartledge, and Andrew P Knights. High-speed performance of a tdfa-band micro-ring resonator modulator and detector. *Optics Express*, 28(11):16845–16856, 2020. → pages 1, 2

[7] Wei Cao, David Hagan, David J Thomson, Milos Nedeljkovic, Callum G Littlejohns, Andy Knights, Shaif-Ul Alam, Junjia Wang, Frederic Gardes, Weiwei Zhang, et al. High-speed silicon modulators for the 2 μm wavelength band. *Optica*, 5(9):1055–1062, 2018. → page 1

[8] Hang Guan, Ari Novack, Tal Galfsky, Yangjin Ma, Saeed Fathololoumi, Alexandre Horth, Tam N Huynh, Jose Roman, Ruizhi Shi, Michael Caverley, et al. Widely-tunable, narrow-linewidth iii-v/silicon hybrid external-cavity laser for coherent communication. *Optics express*, 26(7): 7920–7933, 2018. → page 1

[9] Richard Jones, Pierre Doussiere, Jeffrey B Driscoll, Wenhua Lin, Haijiang Yu, Yulia Akulova, Tin Komljenovic, and John E Bowers. Heterogeneously integrated inp\/silicon photonics: fabricating fully functional transceivers. *IEEE Nanotechnology Magazine*, 13(2):17–26, 2019. → page 1

[10] Alexander N Tait, Thomas Ferreira De Lima, Ellen Zhou, Allie X Wu, Mitchell A Nahmias, Bhavin J Shastri, and Paul R Prucnal. Neuromorphic photonic networks using silicon photonic weight banks. *Scientific reports*, 7 (1):1–10, 2017. → page 1

[11] Q. Cheng, J. Kwon, M. Glick, M. Bahadori, L. P. Carloni, and K. Bergman. Silicon photonics codesign for deep learning. *Proceedings of the IEEE*, 108 (8):1261–1282, 2020. → page 1

[12] Xiaogang Qiang, Xiaoqi Zhou, Jianwei Wang, Callum M Wilkes, Thomas Loke, Sean O'Gara, Laurent Kling, Graham D Marshall, Raffaele Santagati, Timothy C Ralph, et al. Large-scale silicon quantum photonics implementing arbitrary two-qubit processing. *Nature photonics*, 12(9): 534–539, 2018. → page 1

[13] Jacques Carolan, Christopher Harrold, Chris Sparrow, Enrique Martín-López, Nicholas J Russell, Joshua W Silverstone, Peter J Shadbolt, Nobuyuki Matsuda, Manabu Oguma, Mikitaka Itoh, et al. Universal linear optics. *Science*, 349(6249):711–716, 2015. → page 1

[14] Daniel Pérez, Ivana Gasulla, Lee Crudgington, David J Thomson, Ali Z Khokhar, Ke Li, Wei Cao, Goran Z Mashanovich, and José Capmany. Multipurpose silicon photonics signal processor core. *Nature communications*, 8(1):1–9, 2017. → pages 1, 22, 26, 47

[15] Wim Bogaerts, Daniel Pérez, José Capmany, David AB Miller, Joyce Poon, Dirk Englund, Francesco Morichetti, and Andrea Melloni. Programmable photonic circuits. *Nature*, 586(7828):207–216, 2020. → page 1

[16] Christopher V Poulton, Ami Yaacobi, David B Cole, Matthew J Byrd, Manan Raval, Diedrik Vermeulen, and Michael R Watts. Coherent

solid-state lidar with silicon photonic optical phased arrays. *Optics letters*, 42(20):4091–4094, 2017. → page 1

[17] Steven A Miller, You-Chia Chang, Christopher T Phare, Min Chul Shin, Moshe Zadka, Samantha P Roberts, Brian Stern, Xingchen Ji, Aseema Mohanty, Oscar A Jimenez Gordillo, et al. Large-scale optical phased array using a low-power multi-pass silicon photonic platform. *Optica*, 7(1):3–6, 2020. → page 1

[18] David A. B. Miller. Attojoule optoelectronics for low-energy information processing and communications. *J. Lightwave Technol.*, 35(3):346–396, Feb 2017. → page 1

[19] Alexander N. Tait, Hasitha Jayatilleka, Thomas Ferreira De Lima, Philip Y. Ma, Mitchell A. Nahmias, Bhavin J. Shastri, Sudip Shekhar, Lukas Chrostowski, and Paul R. Prucnal. Feedback control for microring weight banks. *Opt. Express*, 26(20):26422–26443, Oct 2018. → page 1

[20] A. H. Ahmed, A. E. Moznine, D. Lim, Y. Ma, A. Rylyakov, and S. Shekhar. A dual-polarization silicon-photonic coherent transmitter supporting 552 gb/s/wavelength. *IEEE Journal of Solid-State Circuits*, 55(9):2597–2608, 2020. → page 1

[21] Guoliang Li, Ying Luo, Xuezhe Zheng, Gianlorenzo Masini, Attila Mekis, Subal Sahni, Hiren Thacker, Jin Yao, Ivan Shubin, Kannan Raj, John E. Cunningham, and Ashok V. Krishnamoorthy. Improving cmos-compatible germanium photodetectors. *Opt. Express*, 20(24):26345–26350, Nov 2012. → page 2

[22] Jurgen Michel, Jifeng Liu, and Lionel C Kimerling. High-performance ge-on-si photodetectors. *Nature photonics*, 4(8):527–534, 2010. → page 2

[23] J Prince, B Draper, E Rapp, J Kronberg, and L Fitch. Performance of digital integrated circuit technologies at very high temperatures. *IEEE Transactions on Components, Hybrids, and Manufacturing Technology*, 3(4):571–579, 1980. → page 2

[24] MW Geis, SJ Spector, ME Grein, RT Schulein, JU Yoon, DM Lennon, S Deneault, F Gan, FX Kaertner, and TM Lyszczarz. Cmos-compatible all-si high-speed waveguide photodiodes with high responsivity in near-infrared communication band. *IEEE Photonics Technology Letters*, 19(3):152–154, 2007. → page 2

[25] Hui Yu, Dietmar Korn, Marianna Pantouvaki, Joris Van Campenhout, Katarzyna Komorowska, Peter Verheyen, Guy Lepage, Philippe Absil, David Hillerkuss, Luca Alloatti, et al. Using carrier-depletion silicon modulators for optical power monitoring. *Optics letters*, 37(22):4681–4683, 2012. → page 2

[26] Yu Zhang, Yu Li, Shaoqi Feng, and Andrew W Poon. Towards adaptively tuned silicon microring resonators for optical networks-on-chip applications. *IEEE Journal of Selected Topics in Quantum Electronics*, 20(4):136–149, 2014. → pages 2, 3

[27] Yu Li and Andrew W. Poon. Active resonance wavelength stabilization for silicon microring resonators with an in-resonator defect-state-absorption-based photodetector. *Opt. Express*, 23(1):360–372, Jan 2015. → pages 2, 3

[28] Sahba Talebi Fard, Kyle Murray, Michael Caverley, Valentina Donzella, Jonas Flueckiger, Samantha M Grist, Edgar Huante-Ceron, Shon A Schmidt, Ezra Kwok, Nicolas AF Jaeger, et al. Silicon-on-insulator sensors using integrated resonance-enhanced defect-mediated photodetectors. *Optics express*, 22(23):28517–28529, 2014. → pages 2, 3

[29] Jianping Yao. Microwave photonics. *Journal of lightwave technology*, 27 (3):314–335, 2009. → page 2

[30] Adil Masood, Marianna Pantouvaki, Guy Lepage, Peter Verheyen, Joris Van Campenhout, Philippe Absil, Dries Van Thourhout, and Wim Bogaerts. Comparison of heater architectures for thermal control of silicon photonic circuits. In *10th International Conference on Group IV Photonics*, pages 83–84. IEEE, 2013. → pages 3, 22

[31] Hasitha Jayatilleka, Kyle Murray, Miguel Ángel Guillén-Torres, Michael Caverley, Ricky Hu, Nicolas AF Jaeger, Lukas Chrostowski, and Sudip Shekhar. Wavelength tuning and stabilization of microring-based filters using silicon in-resonator photoconductive heaters. *Optics express*, 23(19): 25084–25097, 2015. → page 3

[32] Rüdiger Paschotta. Photoconductive detectors. In *Encyclopedia of Laser Physics and Technology*. 2008. → pages 3, 9

[33] Christopher V Poulton, Po Dong, and Young-Kai Chen. Photoresistive microring heater with resonance control loop. In *CLEO: Science and Innovations*, pages SM2I–3. Optical Society of America, 2015. → page 3

[34] Linjie Zhou, Haike Zhu, Heng Zhang, and Jianping Chen. Photoconductive effect on pip micro-heaters integrated in silicon microring resonators. *Optics express*, 22(2):2141–2149, 2014. → page 3

[35] Hasitha Jayatilleka, Hossam Shoman, Lukas Chrostowski, and Sudip Shekhar. Photoconductive heaters enable control of large-scale silicon photonic ring resonator circuits. *Optica*, 6(1):84–91, 2019. → pages 3, 5, 7, 8, 12

[36] Ansys/LUMERICAL. INTERCONNECT. https://www.lumerical.com/products/interconnect/, November 2020. → page 5

[37] JK Doylend, PE Jessop, and AP Knights. Silicon photonic resonator-enhanced defect-mediated photodiode for sub-bandgap detection. *Optics express*, 18(14):14671–14678, 2010. → page 6

[38] Fab: Advanced micro foundry (AMF) silicon photonics fabrication process. https://www.cmc.ca/en/WhatWeOffer/Products/CMC-00200-03001.aspx. Accessed: 2020-04-07. → pages 6, 19, 26

[39] Lukas Chrostowski and Michael Hochberg. *Silicon photonics design: from devices to systems*. Cambridge University Press, 2015. → page 7

[40] Hasitha Jayatilleka. *Enabling practical deployment of silicon ring resonator-based systems*. PhD thesis, University of British Columbia, 2018. → pages 7, 10

[41] Bart Van Zeghbroeck. Principles of semiconductor devices. *Colarado University*, 34, 2004. → page 9

[42] Kasap Safa. *Optoelectronics and Photonics: Principles and Practices*. Pearson Education India, 2009. → page 10

[43] F Gan, T Barwicz, MA Popovic, MS Dahlem, CW Holzwarth, PT Rakich, HI Smith, EP Ippen, and FX Kartner. Maximizing the thermo-optic tuning range of silicon photonic structures. In *2007 Photonics in Switching*, pages 67–68. IEEE, 2007. → page 17

[44] Monireh Moayedi Pour Fard, Glenn Cowan, and Odile Liboiron-Ladouceur. Responsivity optimization of a high-speed germanium-on-silicon photodetector. *Optics Express*, 24(24):27738–27752, 2016. → page 19

[45] David Marpaung, Jianping Yao, and José Capmany. Integrated microwave photonics. *Nature photonics*, 13(2):80–90, 2019. → page 22

[46] Mahmoud S Rasras, Kun-Yii Tu, Douglas M Gill, Young-Kai Chen, Alice E White, Sanjay S Patel, Andrew Pomerene, Daniel Carothers, James Beattie, Mark Beals, et al. Demonstration of a tunable microwave-photonic notch filter using low-loss silicon ring resonators. *Journal of Lightwave Technology*, 27(12):2105–2110, 2009. → pages 22, 26, 47

[47] Suen Xin Chew, Xiaoke Yi, Shijie Song, Liwei Li, Pengju Bian, Linh Nguyen, and Robert A Minasian. Silicon-on-insulator dual-ring notch filter for optical sideband suppression and spectral characterization. *Journal of Lightwave Technology*, 34(20):4705–4714, 2016. → page 22

[48] Shon Schmidt, Jonas Flueckiger, WenXuan Wu, Samantha M Grist, Sahba Talebi Fard, Valentina Donzella, Pakapreud Khumwan, Emily R Thompson, Qian Wang, Pavel Kulik, et al. Improving the performance of silicon photonic rings, disks, and bragg gratings for use in label-free biosensing. In *Biosensing and Nanomedicine VII*, volume 9166, page 91660M. International Society for Optics and Photonics, 2014. → pages 22, 31, 35, 36

[49] Enxiao Luan, Hossam Shoman, Daniel M Ratner, Karen C Cheung, and Lukas Chrostowski. Silicon photonic biosensors using label-free detection. *Sensors*, 18(10):3519, 2018. → pages 22, 31

[50] Bohan Zhang, Kenaish Al Qubaisi, Matteo Cherchi, Mikko Harjanne, Yossef Ehrlichman, Anatol N Khilo, and Miloš A Popović. Compact multi-million q resonators and 100 mhz passband filter bank in a thick-soi photonics platform. *Optics Letters*, 45(11):3005–3008, 2020. → page 22

[51] Patrick Steglich, Siegfried Bondarenko, Christian Mai, Martin Paul, Michael G Weller, and Andreas Mai. Cmos-compatible silicon photonic sensor for refractive index sensing using local back-side release. *IEEE Photonics Technology Letters*, 32(19):1241–1244, 2020. → pages 22, 31

[52] Zeqin Lu, Jaspreet Jhoja, Jackson Klein, Xu Wang, Amy Liu, Jonas Flueckiger, James Pond, and Lukas Chrostowski. Performance prediction for silicon photonics integrated circuits with layout-dependent correlated manufacturing variability. *Optics express*, 25(9):9712–9733, 2017. → page 22

[53] Hossam Shoman, Hasitha Jayatilleka, Anthony HK Park, Ajay Mistry, Nicolas AF Jaeger, Sudip Shekhar, and Lukas Chrostowski. Compact wavelength-and bandwidth-tunable microring modulator. *Optics express*, 27 (19):26661–26675, 2019. → page 22

[54] Long Chen, Nicolás Sherwood-Droz, and Michal Lipson. Compact bandwidth-tunable microring resonators. *Optics letters*, 32(22):3361–3363, 2007. → page 22

[55] Wim Bogaerts, Peter De Heyn, Thomas Van Vaerenbergh, Katrien De Vos, Shankar Kumar Selvaraja, Tom Claes, Pieter Dumon, Peter Bienstman, Dries Van Thourhout, and Roel Baets. Silicon microring resonators. *Laser & Photonics Reviews*, 6(1):47–73, 2012. → pages 23, 24, 34

[56] Meagan N Esbin, Oscar N Whitney, Shasha Chong, Anna Maurer, Xavier Darzacq, and Robert Tjian. Overcoming the bottleneck to widespread testing: A rapid review of nucleic acid testing approaches for covid-19 detection. *RNA*, pages rna–076232, 2020. → page 31

[57] Julian Peto, Nisreen A Alwan, Keith M Godfrey, Rochelle A Burgess, David J Hunter, Elio Riboli, Paul Romer, Iain Buchan, Tim Colbourn, Céire Costelloe, et al. Universal weekly testing as the uk covid-19 lockdown exit strategy. *The Lancet*, 395(10234):1420–1421, 2020. → page 31

[58] A Densmore, D-X Xu, S Janz, P Waldron, T Mischki, G Lopinski, A Delâge, J Lapointe, P Cheben, B Lamontagne, et al. Spiral-path high-sensitivity silicon photonic wire molecular sensor with temperature-independent response. *Optics letters*, 33(6):596–598, 2008. → page 31

[59] Enxiao Luan, Han Yun, Minglei Ma, Daniel M Ratner, Karen C Cheung, and Lukas Chrostowski. Label-free biosensing with a multi-box sub-wavelength phase-shifted bragg grating waveguide. *Biomedical optics express*, 10(9): 4825–4838, 2019. → page 31

[60] Enxiao Luan, Han Yun, Loic Laplatine, Yonathan Dattner, Daniel M Ratner, Karen C Cheung, and Lukas Chrostowski. Enhanced sensitivity of subwavelength multibox waveguide microring resonator label-free biosensors. *Ieee Journal of Selected Topics in Quantum Electronics*, 25(3): 1–11, 2018. → pages 33, 34, 43

[61] Choice of wavelength for rf over fiber – 1310nm vs 1550nm. URL https://www.vialite.com. Accessed: 2020-10-31. → page 36

[62] Joseph A Curcio and Charles C Petty. The near infrared absorption spectrum of liquid water. *JOSA*, 41(5):302–304, 1951. → page 36

[63] Miguel Ángel Guillén-Torres. *Feasibility of optical gyroscopic sensors in silicon-on-insulator technology*. PhD thesis, University of British Columbia, 2015. → page 40

[64] Shankar Kumar Selvaraja, Wim Bogaerts, Philippe Absil, Dries Van Thourhout, and Roel Baets. Record low-loss hybrid rib/wire waveguides for silicon photonic circuits. *Group IV Photonics*, 2010, 2010. → page 40

[65] Hossam Shoman, Hasitha Jayatilleka, Nicolas AF Jaeger, Sudip Shekhar, and Lukas Chrostowski. Measuring on-chip waveguide losses using a single, two-point coupled microring resonator. *Optics Express*, 28(7):10225–10238, 2020. → page 47